



universität  
wien

# DIPLOMARBEIT

Titel der Diplomarbeit

**Fluorescence detection of far-field diffraction with  
large molecules**

Verfasserin

**Adriana Milic**

angestrebter akademischer Grad

**Magistra der Naturwissenschaften (Mag. rer. nat.)**

Wien, 2012

Studienkennzahl lt. Studienblatt:	A 411
Studienrichtung lt. Studienblatt:	Diplomstudium Physik UniStG
Betreuerin / Betreuer:	Univ. Prof. Dr. Markus Arndt



# Kurzfassung

In dieser Diplomarbeit wird der Aufbau eines Materiewellen Fernfeld-Interferometers mit Detektion der Interferenzmuster über Fluoreszenzmikroskopie diskutiert.

Das Ziel des Experiments ist es, den Welle-Teilchen Dualismus für große organische Moleküle zu zeigen und ein intuitives Bild des Welle-Teilchen Dualismus zu erhalten. Die hohe Empfindlichkeit unserer Detektionsmethode ermöglicht die Detektion einzelner Moleküle, womit deren Teilchencharakter gezeigt ist. Das Interferogramm, welches durch Beugung an materiellen Gittern entsteht, zeigt gleichzeitig den Wellencharakter der Teilchen. Deshalb liefert dieses Experiment einen pädagogisch wertvolles Resultat, da auf einen Schlag Wellen- und Teilcheneigenschaft eindeutig gezeigt werden.

Die Beugungsgitter, die für dieses Experiment verwendet wurden, sind teilweise nur 10 nm dick. Gitter von dieser geringen Dicke wurden nie zuvor in einem Fernfeld Beugungsexperiment mit großen Molekülen verwendet. Die van der Waals Kräfte zwischen den Gittern und den Molekülen sind Gegenstand aktueller Experimente.



# Abstract

In this thesis the setup of a far-field matter wave interferometer with a fluorescence microscopy detection scheme is discussed.

The experiment aims at revealing the quantum nature of large organic molecules. Furthermore, it provides an intuitive proof of the wave-particle duality. The high sensitivity of the detection scheme allows single molecule detection, giving evidence for the particle nature of the molecules. The detected interferogram reveals the wave nature of the molecules by demonstrating the superposition principle.

Hence, the experiment gives a pedagogically valuable result by showing the wave and the particle characteristics of molecules at the same time.

In addition, the nanostructured diffraction gratings used in this experiment are as thin as 10 nm. Such material gratings have never been used in far-field diffraction with large molecules and offer new possibilities for investigation such as the van der Waals force acting between the molecules and the diffraction grating.



# Contents

<b>1</b>	<b>Introduction</b>	<b>9</b>
1.1	Motivation . . . . .	9
1.2	Matter waves . . . . .	11
1.3	Coherence and far-field diffraction . . . . .	13
1.4	Interferometry with matter waves . . . . .	15
<b>2</b>	<b>Experimental setup</b>	<b>19</b>
2.1	Transversal collimation slits . . . . .	21
2.2	Velocity selection . . . . .	23
2.3	Source . . . . .	25
2.4	Detection surface . . . . .	30
2.5	Quartz balance . . . . .	33
2.6	Gratings . . . . .	33
2.6.1	Grating with 170 nm thickness . . . . .	33
2.6.2	Gratings with 10 nm thickness . . . . .	34
2.7	Electron multiplying CCD camera . . . . .	35
2.8	Lasers . . . . .	39
2.8.1	660 nm laser . . . . .	40
2.8.2	445 nm laser . . . . .	40
<b>3</b>	<b>Fluorescence</b>	<b>43</b>
3.1	Fluorescence mechanism . . . . .	43
3.2	Quantum yield . . . . .	44
3.3	Fluorescence lifetime . . . . .	44
3.4	Fluorescence quenching . . . . .	45
3.5	Bleaching and blinking . . . . .	46

<b>4</b>	<b>Molecules</b>	<b>49</b>
4.1	Tetraphenylporphyrine- TPP . . . . .	49
4.1.1	TPPF <sub>84</sub> . . . . .	50
4.2	Rhodamine B . . . . .	51
4.3	Phthalocyanine . . . . .	52
4.4	Velocity and mass spectra . . . . .	54
<b>5</b>	<b>Fluorescence surface detection</b>	<b>59</b>
5.1	Imaging . . . . .	59
5.2	Background signal . . . . .	60
5.2.1	Stray light . . . . .	63
5.2.2	Dark counts from the EMCCD . . . . .	65
5.3	Plasma cleaning . . . . .	66
5.4	Molecular number density . . . . .	73
<b>6</b>	<b>Interferograms</b>	<b>75</b>
6.1	Single molecule detection . . . . .	76
6.2	Van der Waals interaction . . . . .	79
6.3	Gravitational acceleration . . . . .	82
<b>7</b>	<b>Results</b>	<b>83</b>
7.1	Thin gratings . . . . .	83
7.1.1	Opening fraction $f=0.5$ . . . . .	83
7.1.2	Opening fraction $f=0.8$ . . . . .	84
7.2	Thickness 170 nm, opening fraction 0.75 . . . . .	86
<b>8</b>	<b>Outlook</b>	<b>91</b>
<b>9</b>	<b>Danksagung</b>	<b>99</b>
<b>10</b>	<b>Curriculum Vitae</b>	<b>101</b>



# 1 Introduction

## 1.1 Motivation

In 1924 in his thesis *Recherches sur la théorie des Quanta* Louis De Broglie came up with the groundbreaking idea to describe massive particles by their wavelength characteristics [1].

Thus, the particle wave duality can be extended from photons to any massive particle. The so-called De Broglie wavelength is given by

$$\lambda_{DB} = \frac{h}{p} = \frac{h}{mv} \quad (1.1)$$

where  $h=6.626 \cdot 10^{34}$  Js is the Planck's constant,  $m$  the mass of the particle and  $v$  its velocity. De Broglie's theory was experimentally confirmed by Lester Germer and Clinton Davisson in 1927 by sending electrons on a nickel target and looking at the diffraction pattern, which matched with the predictions of De Broglie's theory [2].

In 1924 the concept of the wave-particle duality was not new in case of photons.

In 1905, Einstein found an explanation for the photoelectric effect by assuming that light consists of particles which carry energy only dependent on their frequency  $\omega$ . The experimental observation was the following: electrons are emitted from a material by absorbing energy from electromagnetic radiation. The electrons' maximal kinetic energy is dependent on the frequency of the incident photon. It is given by:

$$E_{\text{kin}}^{\text{max}} = \hbar\omega - W \quad (1.2)$$

where  $W$  gives the minimum energy required to remove an electron from the material's surface.

Einstein's particle interpretation of light was not a new concept. Since Isaac Newton's corpuscle theory it was believed that light consists of particles.

## 1 Introduction

In 1802 Thomas Young showed by his double slit experiment that light performs interference effects, only explicable by its wave nature [3].

Both, the double slit experiment and the photoelectric effect are experimental facts and thus, Einstein and Young must be right. Light shows wave and particle properties and it depends on the experiment which one is revealed.

De Broglie took a further step and predicted that also the electron, a massive particle, shows wave properties.

Since then a lot of experiments have been carried out proving that massive particles have wave properties, or more precisely, obey the superposition principle. More details on those experiments are in section 1.3.

The far-field diffraction experiments this thesis is about were done with gratings of different thicknesses and opening fractions, which allowed us not only to reduce the van der Waals forces with decreasing grating thickness, but also to draw conclusions about the van der Waals forces acting between the grating and the molecules (chapter 6). More information about the gratings can be found in section 2.6.

As described in chapter 5 and 6, we had to improve our understanding of the electron multiplying CCD (EMCCD) camera employed in this experiment in order to reach single molecule sensitivity. It was crucial to decrease the background in the detection area in order to be able to see single particles (section 5.2). This was achieved by using a laser with a wavelength of 661 nm and molecules with a high extinction coefficient. In chapter 4 the molecules we used are characterized. Chapter 2 is about the experimental setup. Among other things the employed lasers are described there (section 2.8). Chapter 3 is on the fluorescence mechanism in general.

One of the main aims of this experiment was to show an intuitive evidence for the quantum nature of large molecules. Combining this with single molecule detection (described in section 6.1) which allows seeing the particles arriving one by one at the screen and gradually building up the interference pattern gives an intuitive picture of both the wave and particle nature of the used molecules and a straightforward proof of the wave-particle duality.

Another observation was the decomposition and recombination of Rhodamine B in our source, which we were only able to reveal due to the separation between the interference maxima. The molecule's mass measured in the Time Of Flight spectrometer (TOF) was the expected one due to the afresh decomposition by ionization. Further details on this observation are provided in chapter 4 and 6.

## 1.2 Matter waves

From Planck's formula  $E=\hbar\omega$  and equation 1.1 follows that the first part of De Broglie's equation is true for light.

The basic equation of non-relativistic quantum mechanics which describes the behaviour of quanta, thus of massive and light particles, is the Schrödinger equation. It can be written in stationary (1.4) and time dependent (1.3) form:

$$i\hbar\frac{\partial}{\partial t}\Psi(\vec{x},t) = \left(-\frac{\hbar^2}{2m}\Delta + V\right)\Psi(\vec{x},t) \quad (1.3)$$

$$H\Psi(\vec{x},t) = E\Psi(\vec{x},t) \quad (1.4)$$

A particle for which those equations are true can be described by a wave packet

$$\Psi(\vec{x},t) = \frac{1}{2\pi} \int_{-\infty}^{\infty} \Phi(\vec{k}) e^{i(\vec{k}\vec{x}-\omega t)} d\vec{k}. \quad (1.5)$$

A wave packet is the superposition of plane waves with different frequencies. The stronger it is localized, the more frequencies are needed to allow constructive interference.

Its group velocity is given by

$$v_{\text{group}} = \frac{\partial\omega}{\partial k}. \quad (1.6)$$

$\omega$  is the wave's angular frequency and  $k$  the wavenumber.

In case of matter waves we can insert eq. 1.2 and  $p = \hbar k$  and obtain

$$\frac{\partial(E/\hbar)}{\partial(p/\hbar)} = \frac{\partial \frac{1}{2} p^2}{\partial p} = \frac{p}{m} = v \quad (1.7)$$

$p$  is the particle's momentum,  $m$  its mass and  $v$  its velocity.

If in the dispersion relation  $\omega(k)$  the angular frequency  $\omega$  is directly proportional to

## 1 Introduction

$k$ , then the group velocity equals the phase velocity

$$v_{\text{phase}} = \frac{\omega}{|\vec{k}|}. \quad (1.8)$$

If group and phase velocity are not equal, the envelope of the wave packet

$$\Phi(\vec{k}) = \frac{1}{2\pi} \int_{-\infty}^{\infty} \Psi(\vec{x}, 0) e^{-i\vec{k}\vec{x}} d\vec{k} \quad (1.9)$$

will become distorted as the wave propagates.

Separating the variables we obtain

$$\Psi(\vec{x}, t) = e^{-i\omega t} \Phi(\vec{x}). \quad (1.10)$$

By inserting eq. 1.10 into the wave equation

$$\left( \nabla^2 - \frac{1}{c^2} \frac{\partial^2}{\partial t^2} \right) \Psi(\vec{x}, t) = 0 \quad (1.11)$$

we obtain

$$\frac{\nabla^2 \Phi}{\Phi} = \frac{1}{c^2 T} \frac{d^2 T}{dt^2}. \quad (1.12)$$

The left side depends only on  $\vec{x}$ , the right side on  $t$ . In the general case it is only valid if both sides equal to a constant value. For  $\Phi(\vec{x})$  we obtain:

$$\frac{\nabla^2 \Phi}{\Phi} = -k^2 \quad (1.13)$$

Without loss of generality, we set the value  $-k^2$  as the constant. After rearranging eq. 1.13, we obtain the Helmholtz equation

$$\nabla^2 \Phi(\vec{x}) + k^2 \Phi(\vec{x}) = (\nabla^2 + k^2) \Phi(\vec{x}) = 0 \quad (1.14)$$

From the Helmholtz equation follows that matter waves and light waves can be described by the same equations in the stationary case. In case of time dependent phenomena a different behaviour is obtained. [4, 5]

## 1.3 Coherence and far-field diffraction

Crucial for interference is the transversal and longitudinal coherence length of a matter wave [6].

Two waves from adjacent slits are coherent if they have a fixed phase relation. In order to obtain an interference pattern at least two adjacent slits of the grating have to be illuminated coherently.

For diffracting ten times larger particles the grating constant must be ten times smaller, if the velocity stays approximately the same. Since sources for large and slow molecules are experimentally still challenging, one has to move closer to the interference grating, to the so-called near field, for doing interference experiments with much larger molecules. Speaking more precisely, one has to be within the Talbot length given by

$$L_T = \frac{2d^2}{\lambda_{DB}} \quad (1.15)$$

to obtain near-field diffraction. Here,  $d$  is the width of the window the grating is written in.

Since the width of the molecular beam is finitely small, there are several emitter locations (which leads to a transverse shift of the interference pattern) and hence, a smearing over the minima and maxima of the interferogram. In far-field diffraction transversal decoherence can be avoided, if the divergence angle  $\Theta_{\text{div}}$  of the beam is much smaller than the diffraction angle  $\Theta_{\text{diff}}$ .  $\Theta_{\text{div}}$  and hence, the transversal coherence is determined by the width of the first collimation slit.

If the condition

$$a_{\text{coll}} \ll \frac{\lambda_{DB}}{2\sin\Theta_{\text{diff}}} \quad (1.16)$$

where  $a_{\text{coll}}$  is the width of the first collimation slit, is met, transversal coherence is given.

In our experiment the transversal coherence length is in the range of few micrometers since the wavelength is in the range of picometers and the slit width of the transversal collimation slits was varied from one to five micrometers.

## 1 Introduction

The longitudinal coherence length is given by

$$l_{\text{long.}} = \frac{\lambda_{DB}^2}{\Delta\lambda} = \frac{m^2}{h^2} \cdot dv \quad (1.17)$$

In our setup the thermal velocity spread for most molecules was about 60 m/s and the mass was about  $10^{-25}$ kg. Hence, the coherence length is about 10-100 pm.

Far-field diffraction or also Fraunhofer diffraction is the most intuitive way of seeing the superposition of waves and therefore understanding one of the most important principles of quantum mechanics. As long as the wave fronts can be considered as plane waves, the diffraction is considered as far field diffraction (fig. 1.1).

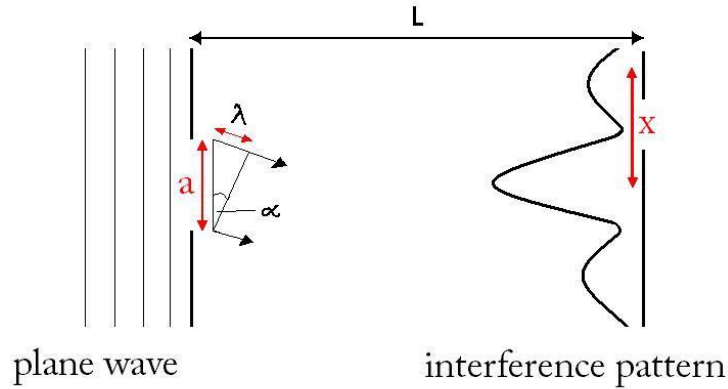


**Figure 1.1:** A plane wave is diffracted on a slit and detected in a distance which is much larger than the slit width. The diffraction angle is given by  $\sin\alpha = \lambda_{DB}/a$  where  $a$  is the slit width and  $\lambda_{DB}$  the De Broglie wavelength. The separation  $x$  between the interference maxima is given by  $L \cdot \lambda_{DB}/a$  for small angles.

For diffraction on a grating the following equation is true for the  $n$ -th order interference maximum:

$$g \cdot \sin\phi = n \cdot \lambda_{DB} \quad (1.18)$$

where  $\phi$  is the diffraction angle and  $g$  the grating constant. For small angles  $\sin\phi \approx \phi = \frac{\lambda_{DB}}{g}$ . The separation  $x$  between the zeroth and the first order maximum is given by

$$x = \sin\phi \cdot L \quad (1.19)$$

and hence

$$x = L \cdot \frac{\lambda_{DB}}{g}. \quad (1.20)$$

The De Broglie wavelength of the molecules used in this experiment is in the picometer range. Therefore, the resolution we had to achieve in order to be able to differentiate between the single interference maxima had to be in the micrometer range.

## 1.4 Interferometry with matter waves

It is known today that the double-slit experiment, which was first performed with light, can also be carried out with massive particles. The question arises why further experiments with matter waves shall be performed when the concept of wave-particle is already verified. It should be emphasized that the scientific question whether quantum physics applies to all mass and complexity scales is an open one. Superposition of macroscopic objects is not observed in our everyday life. The question whether the transition from quantum to classical physics is a sudden one or the result of the increasing coupling of a quantum object with the environment, which results in loss of coherence, a crucial condition for observing quantum phenomena, has not been answered yet either.

Matter wave interferometers can provide answers to these questions by interfering much more massive particles that have ever showed quantum behaviour before.

The first matter wave experiments, verifying De Broglie's theory, were performed with electrons [2]. In 1930 the first diffraction experiments with Helium atoms and H<sub>2</sub> molecules were accomplished [7] and shortly afterwards Halban and Preiswerk showed diffraction of neutrons [8].

Brockhouse and Shull [9] scattered neutrons on condensed matter in order to study its structure and about thirty years later fundamental quantum effects were studied by neutron double-slit diffraction [10, 11].

Since the wavelength is inversely proportional to the particles mass, the experimental effort increases with larger getting mass. Interference slits or gratings have to become smaller and a higher isolation from the environment is required to account for the shorter De Broglie wavelength and to avoid decoherence due to collisions with background gases.

## 1 Introduction

After the development of more sophisticated techniques which allowed i.e. the production of gratings with smaller grating constants which are suitable for experiments with more massive molecules and with the invention of the laser which allowed to cool atoms and detect molecules, matter wave interferometry moved on to more massive particles and became an important tool of investigation for molecule metrology and molecule lithography .

For example, the electric polarizability of sodium was measured by Ekstrom et al. in an atom interferometer [12], the rotation of the earth was measured accurately using an atom interferometer gyroscope [13] and Grisenti et al. [14] determined the bond length and energy of the fragile He<sub>2</sub> dimer.

So far, three interferometer types for molecules have been built. In 1994, a Ramsey-Bordé interferometer where I<sub>2</sub> was diffracted on laser light, was realized [15]. A mechanical Mach-Zehnder interferometer with Na<sub>2</sub> dimers was built by Chapman et al. in 1995 [16] and in 2002, a Talbot-Lau experiment was accomplished for diffracting C<sub>70</sub> molecules [17].

An interferometer for large molecules allows to move closer to the border of quantum mechanics and classical physics. It also enables us to approach decoherence mechanisms as described in [18, 19, 20].

Furthermore, matter wave interferometry already lead to several results in molecule metrology and molecule lithography [21, 22].

A further step in interferometry with big molecules was done in 1999 by diffracting C<sub>60</sub> molecules, so called fullerenes or bucky balls. Those particles which have a mass of about 720 amu were diffracted on a grating with a period of 100 nm [23].

The interference pattern was scanned by an ionizing focused laser beam. In this experiment the fullerenes had an average velocity of about 100 m/s. Hence, the De Broglie wavelength is around 5 pm. Although the diameter of the molecule is about 7Å, hundred times bigger than the De Broglie wavelength, interference could be observed. Up to that time, C<sub>60</sub> was the most complex and massive object for which wave behaviour



had been observed. Due to its many excited internal degrees of freedom and their possible couplings to the environment, which lead to decoherence, it is almost a classical body.

It should be pointed out that molecule interference is a single particle phenomenon. The average distance between the molecules when leaving the thermal source is  $100\ \mu\text{m}$ . The van der Waals radius is  $10^4$  times smaller than that and hence, there is no interaction between the molecules. Therefore, each molecule must be interfering with itself.

The most massive particles for which interference was shown have masses of up to  $6910\ \text{amu}$  and a size of maximal  $60\ \text{\AA}$ . The diffraction was performed with the Kapitza-Dirac-Talbot-Lau interferometer [24].

Considering the historical development of the interference experiments with increasingly heavy particles, the question arises whether there is a mass limit for the validity of quantum mechanics. The quantum theory itself does not predict any limit in mass. It is more likely that revealing the quantum nature of massive objects is only a technical challenge.

There are also theoretical predictions for the mass limits of quantum mechanics. In [25, 26], the lower bound for the mass is at a mass of  $10^5\ \text{amu}$ . Hence, for larger particles interference should be unobservable.



## 2 Experimental setup

The far-field interferometer is divided into three chambers. In fig. 2.1 the setup scheme can be seen. A picture of the setup can be seen in fig. 2.2.

The source is located in the oven chamber. In order to be able to know the relative amount deposited on the detection surface or if there were any molecules evaporated, we mounted a quartz balance in front of the oven with an offset of 3.5 cm. The profile of the beam follows a  $\cos^2(x)$  function.

According to that we could calculate back from the amount arriving on the quartz balance to the amount of molecules being emitted at the center of the beam. From that the amount arriving at the detection surface on the other end of the interferometer chamber was deduced.

In the main chamber there are two collimation slits and the interference grating. In addition to the transversal collimation slits we also have two horizontal velocity selection slits with different widths ranging from 60  $\mu\text{m}$  to 450  $\mu\text{m}$  build in in the chamber. We can move them completely out of the beam, if necessary.

The interference gratings made of silicon nitride were fabricated by Ori Chesnovsky and Alexander Tsukernik at the University of Tel Aviv. We also used older silicon nitride gratings with a thickness of 170 nm fabricated at MIT by Tim Savas, which were already used in former experiments.

Three gratings are mounted on the grating holder in the vacuum chamber. This way, we could exchange the gratings during the experiment as it was needed.

The main chamber is separated from the oven chamber and the detector chamber by two valves. The quartz plate which is coated like a dichroic mirror is attached to one end of this chamber. The molecules deposited here are detected via a fluorescence microscopy detection scheme. The optical path can be seen in fig. 2.1.

## 2 Experimental setup

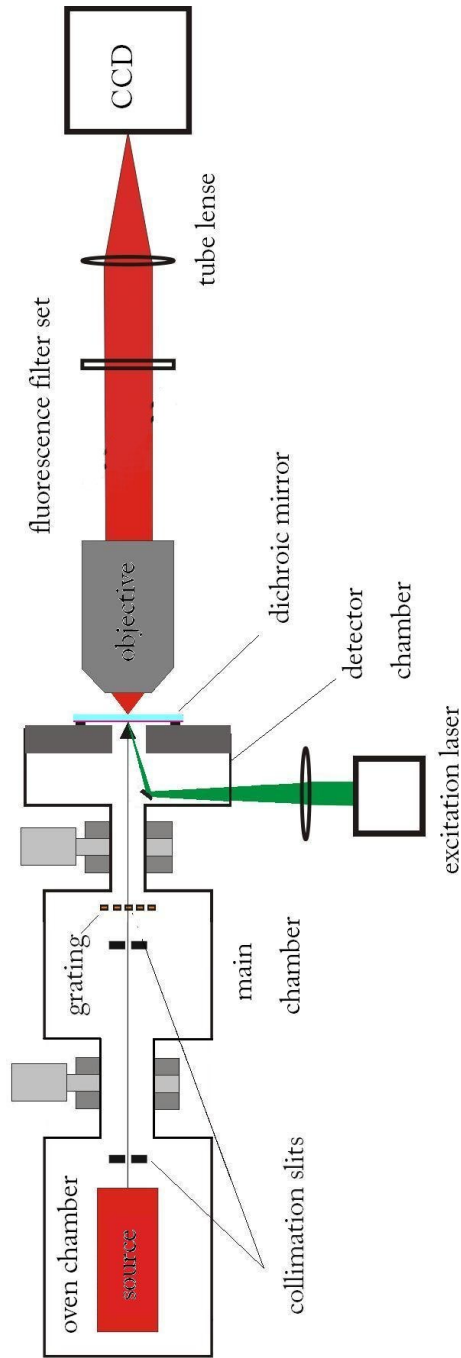


**Figure 2.1:** Scheme of the experimental setup: In the oven chamber the source evaporating the molecules is located. In the meanwhile it was replaced by a laser evaporation source. The main chamber where the collimation slits and the interference grating is located is separated from the oven and the detector chamber by two valves. The quartz plate where the molecules are deposited is attached to the detector chamber. The interference pattern is illuminated from the inside of the chamber by a laser which enters the vacuum chamber through a window. The dichroic mirror is a quartz plate coated on the vacuum side. It reflects the laser light (we used 532 and 445 nm excitation lasers with this setup scheme), but transmits the fluorescence light of the molecules. The fluorescence light is collected by an objective and imaged by a cooled EMCCD camera.

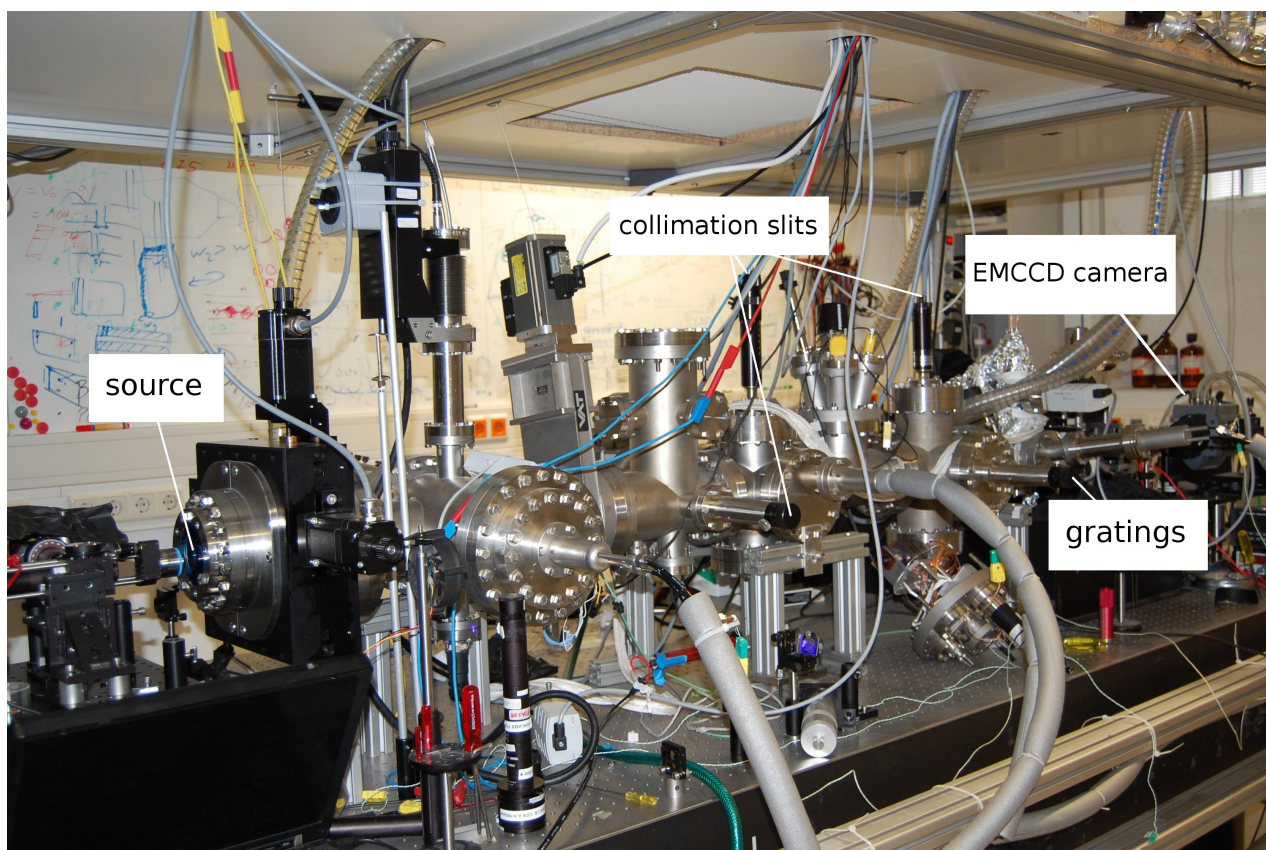


**Figure 2.2:** Experimental setup: The source in this picture is the new implemented laser evaporation source. The position of one transversal and two horizontal collimation slits is indicated. Three gratings are mounted on a feedthrough, so, they can be exchanged without opening the vacuum chamber. In the back of the picture the cooled EMCCD camera can be seen.

When using the 532 or the 445 nm laser (this was depending on the molecule evaporated), the sample was illuminated from the inside of the chamber. The green and blue laser were used for excitation of TPP and Rhodamine B. With the red laser the Phthalocyanines were excited (here, also the setup scheme differed). Once the molecules were deposited they were illuminated and emitted fluorescence light which was collected by an objective positioned on the other side of the quartz sample. The molecules were then imaged by a cooled EMCCD camera (Andor Solis DV885).

## 2.1 Transversal collimation slits

The collimation slits are piezo-driven and can be moved with an accuracy of  $\pm 0.01 \mu\text{m}$  width. In order to reduce the van der Waals interaction with the molecules, the

## 2 Experimental setup

diameter of the slit edges was reduced. The original piezo-driven slits were replaced by razor blades which have a diameter of 200-250 nm (left picture in fig. 2.3).

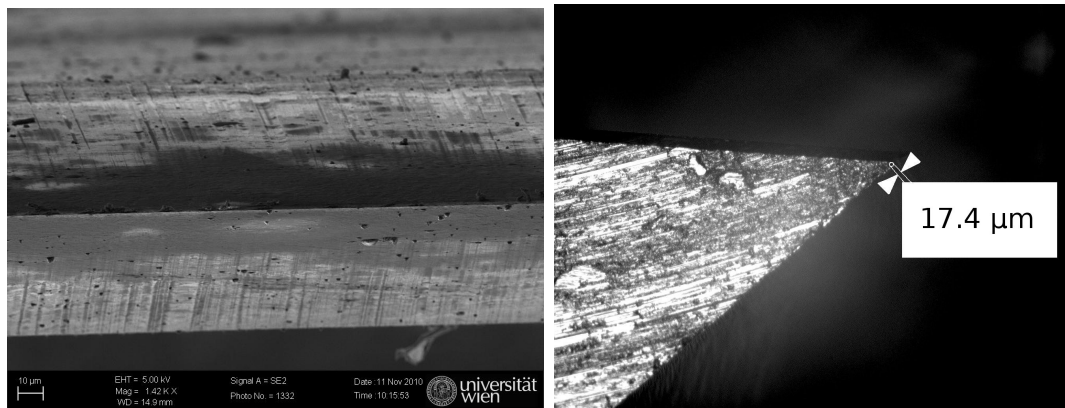


**Figure 2.3:** The left picture was taken in an scanning electron microscope (SEM) and shows the edge of the razor blade used for the collimation slit. It has a diameter of 200-250 nm. The diameter of the slits originally mounted was measured in an optical microscope (right picture). It was determined to be about 17  $\mu\text{m}$ .

The edges of the Piezo Jena slits originally mounted had a diameter of 15-20  $\mu\text{m}$  (right picture in fig. 2.3). Hence, the diameter was reduced by a factor of 50.

By changing the slits we aimed at reducing the van der Waals interaction between the slits and the molecules which are passing through. The van der Waals force imposes a phase shift on the molecule passing the grating and thus, leads to a smearing of the interference pattern. Furthermore, the effective slit width is reduced and hence, the signal decreased.

Before mounting the blades on the slits, they had to be checked for holes and uneven edges. First, one razor blade was put onto the old blade of the slit and fixed by a magnet. The other blade was put next and fixed by a magnet as well. The blades had to be handled with great care, because when dropping or touching them the edges got uneven. With the optical microscope the razor blades were adjusted to each other. On a length of about 1 cm we wanted their separation to vary by only one or two micrometers. After the adjustment the blades were glued to the old blades and the magnets were removed.

Then, the slits were placed into the SEM and the variation of the separation of the blades was checked at two positions (fig. 2.4).

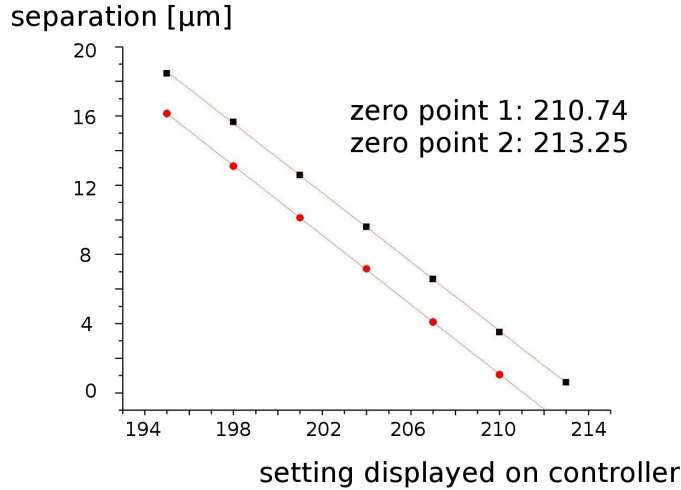


**Figure 2.4:** Variation of the separation of one collimation slit at two points about 1 cm apart from each other. We adjusted the slits as parallel to each other such that the variation was less than  $2 \mu\text{m}$ . At one end of the slit the point at which the blades were entirely closed was 210.74, at the other end 213.25. We took the mean of the two points, hence 212, as zero point of the collimation slit.

As both collimation slits were mounted on a rail, they could be adjusted perpendicular to the rail and parallel to the direction of gravitation outside the chamber. The adjustment was done with a laserpointer by diffracting the light on the slit and obtaining the interference pattern. This method allowed to adjust the slits to an accuracy of less than 5 mrad.

## 2.2 Velocity selection

In earlier Talbot-Lau experiments [27] the molecular velocity spread  $\Delta v/v$  was about 10 %. In those setups it was necessary to have a quite narrow velocity distribution in order to see high contrast interference fringes. This was achieved by selecting certain free flight parabolas of the molecules in the earth's gravitational field using three horizontally oriented slits.

In our experiment the oven orifice was very big compared to the horizontal collimation slits. Therefore, a horizontal collimation slit was placed just after the first transversal collimation slit about 0.7 m away from the oven. The second velocity selection slit was placed 1.15 m away from the oven. After moving all the collimation slits in the beam

## 2 Experimental setup

the thermal velocity spread could be reduced from 60 % to about 20-30 %.

Fast molecules arrive at the top of the detection surface, while slower ones which have more time to fall reach the slide at a lower position. Therefore, our method allows to select the longitudinal coherence length a posteriori, after the deposition. In the present configuration the width of the velocity distribution is essentially determined by the size of the slits.

In order to obtain the velocity distribution for the height at which the molecules arrive at the quartz slide, we have to consider fig. 2.5.

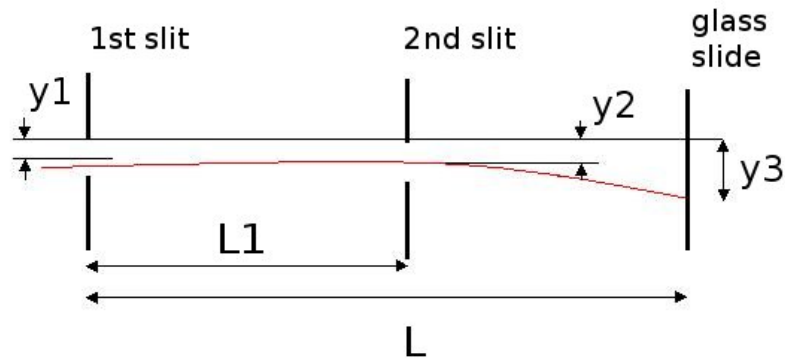


**Figure 2.5:** In the direction of gravity the molecular beam is confined by two horizontal collimation slits, here indicated as 1st and 2nd slit. The orifice of the oven is very big in diameter compared to the velocity selection slits and cannot be taken as third reference point of the flight parabola. The velocity is calculated as a function of the height at which the molecules arrive on the quartz slide ( $y_3$ ), the heights of the two collimation slits ( $y_1$ ,  $y_2$ ) and the distances  $L$  and  $L_1$ .

The equations of motion for the molecules for the heights  $y_2$  and  $y_3$  are

$$y_2 = -\frac{gt_2^2}{2} + v_y t_2 + y_1 \quad (2.1)$$

$$y_3 = -\frac{gt_3^2}{2} + v_y t_3 + y_1 \quad (2.2)$$

where  $v_y$  is the velocity in direction of gravitation,  $t_2=L_1/v$  and  $t_3=L/v$  are the times the molecules need to fly the distances  $L$  and  $L_1$ .  $v$  is the longitudinal velocity of the molecules.



By subtracting eq. 2.1 from eq. 2.2, multiplying eq. 2.1 by  $L/L_1$  and rearranging the terms, we obtain

$$v = \sqrt{\frac{-g/2(L^2 - L_1 \cdot L)}{y_3 - y_2 - L/L_1(y_1 - y_2)}} = \sqrt{\frac{A}{y_3 - B}} \quad (2.3)$$

The parameter A can be calculated from the distances L and  $L_1$ . B which corresponds to the height to which the fastest molecules are flying can be obtained by fitting the function 2.3 to the data.

After obtaining B we can select molecules of a certain velocity interval by selecting the height at which they arrive. From the height the velocity distribution is calculated.

For seeing higher order interference fringes a better velocity selection is needed. This can be accomplished by using a chopper. The chopper we currently have would reduce the velocity spread to 15 %.

## 2.3 Source

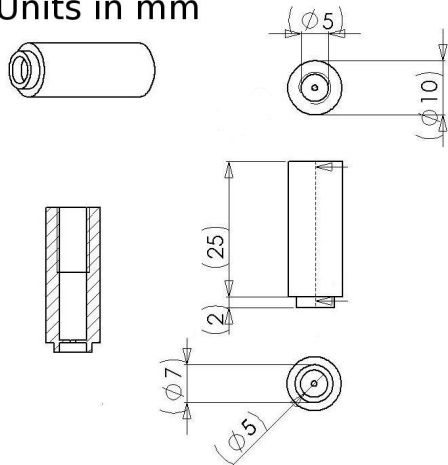
The source is a hollow, resistively heated copper cylinder which is filled with molecules (see left picture in fig. 2.6). The diameter of the hole is around 400  $\mu\text{m}$  (right picture in fig. 2.6), so the emitted beam is very big compared to the collimation slits. Since the oven orifice is a bit off the center, we put a mark on the oven and inserted it in its heating spool with the mark on the top. In this way we ensured that the beam is always emitted from the same position.

The temperature was measured at the heating spool in front of the oven orifice. By knowing the evaporation point of the molecules filled in the oven we could conclude when they got into the gasphase. If the temperature matched with the flux shown on the quartz balance, there was a proper molecular beam.

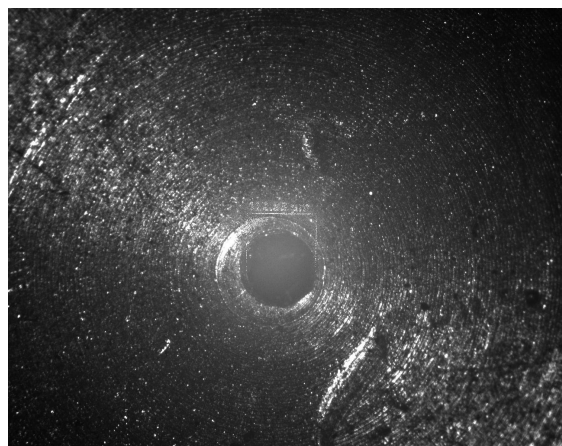
The whole oven flange is mounted on a x-y-stage. In this way the position of the beam could be optimized in relation to the quartz plate. This was done by depositing a certain amount of molecules on the quartz plate, shifting the oven and again depositing the same amount. In this way we could find the optimal position in order to waste as little of the molecules as possible. The beam's  $\cos^2(x)$  profile was also measured (x is the position vertical to the beam), as can be seen in figure 2.7).

## 2 Experimental setup

Units in mm



2.6.1



2.6.2

**Figure 2.6:** The thermal source we used for this experiment was made of copper. The technical drawing is shown in the left picture. The diameter of the orifice was measured in the optical microscope and was determined to be  $400 \mu\text{m}$ . After filling in the molecules the source was closed by a screw.

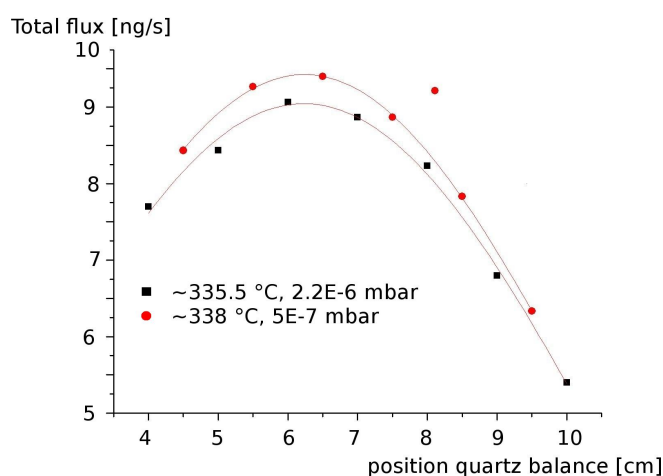


**Figure 2.7:** We measured the beam profile for TPP for 2 different temperatures as given in the graph. Although the temperature difference was just  $2.5 \text{ }^\circ\text{C}$ , the pressure increased by a factor of 5 due to the fact that the melting point of TPP is at  $335 \text{ }^\circ\text{C}$ . The flux was 5 % lower at the lower temperature.

In order to acquire the fluorescence parameters we need an estimation for the number of particles the source is emitting. The molecular flux is related to the pressure inside

the oven. This relation depends on the condition of the gas flow [28], which again depends both on the molecular free path in the oven and the oven dimensions.

Where the mean free path  $\Lambda$  exceeds the dimensions of the oven orifice, the number and angular distribution of the emerging particles can be calculated from the kinetic gas theory [29]. The number of particles in the forward direction per steradian per second is given by

$$I = \frac{n_0}{2\pi} \sqrt{\frac{2k_B T}{\pi m}} S \left[ \frac{\text{molecules}}{\text{sr} \cdot \text{s}} \right] \quad (2.4)$$

where  $n_0$  is the number of molecules per volume ( $n_0=N/V$ ),  $k_B$  is the Boltzmann constant,  $m$  is the mass of the particular molecule,  $T$  the temperature of the oven and  $S$  the aperture area. If we consider the gas inside the oven as an ideal gas, the pressure  $p$  is given by  $p=n_0 k_B T$  and the particle flux at the detector can be written as

$$I = \frac{p}{2k_B T \pi} \sqrt{\frac{2k_B T}{\pi m}} S = \quad (2.5)$$

$$8.389 \times 10^{23} \cdot \frac{p}{\sqrt{MT}} S \left[ \frac{\text{molecules}}{\text{sr} \cdot \text{s}} \right]. \quad (2.6)$$

$M[\text{amu}]$  is the molecular weight, related to the mass  $m[\text{kg}]$  as follows:

$$m[\text{kg}] = M[\text{amu}]/(1000 \cdot N_A) \quad (2.7)$$

Hence, the flux of molecules is given by

$$N_{mol} = 8.389 \times 10^{23} \cdot \frac{p[\text{Pa}]}{\sqrt{M[\text{amu}]T[\text{K}]}} \frac{S}{r^2} \left[ \frac{\text{molecules}}{\text{m}^2 \text{s}} \right] \quad (2.8)$$

where  $r$  is the distance between the oven notch and the detection surface.

When the mean free path is much smaller than the diameter of the orifice ( $\Lambda < 0,1d$ ), the flux rate is given by

$$\left( \frac{dN}{dt} \right)_a = \left( \frac{2}{\gamma + 1} \right)^{\frac{\gamma+1}{2(\gamma-1)}} \sqrt{\frac{\gamma}{k_B m}} \frac{p}{\sqrt{T}} S. \quad (2.9)$$

as described in detail in [30, 31].

Here,  $\gamma = C_p/C_v$  is the adiabaticity parameter. The vapor pressure is given by the

## 2 Experimental setup

Clausius-Clapeyron equation

$$p = Ae^{-\frac{B}{T}}. \quad (2.10)$$

A and B are experimental parameters. B is related to the molar sublimation enthalpy  $H_{sub}$  by the gas constant  $R = 8.3145 J/(mol \cdot K)$ :

$$B = \frac{H_{sub}}{R} \quad (2.11)$$

Hence, when knowing B we can extract  $H_{sub}$  by measuring the temperature dependence of the fluorescence signal, which is proportional to the molecular beam density.

By adding a glass capillary array in front of the oven notch, we reduced the loss of molecules and focused the beam [32]. The capillary array is a 2 mm thick glass plate with holes which are 20  $\mu\text{m}$  in diameter, as shown in fig. 2.8. When a molecule enters a hole, it is reflected from the walls of the hole, if it is not flying straight towards the forward direction. In this way the molecules are directed in the forward direction and the molecular beam is getting narrower.

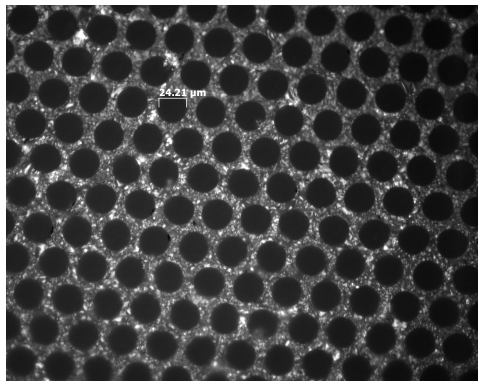


**Figure 2.8:** A picture of the glass capillary array taken with the optical microscope. The diameter of the holes was determined to be 20  $\mu\text{m}$ .

We measured the distribution of the molecules evaporated from the oven with and without the capillary array and compared the beam profiles (fig. 2.9). As shown in the graph the distribution did get a lot narrower. The full width half maximum of the beam decreased by a factor of 2. The flux decreased effectively (in the graph the fluxes are normed to 1) from 0.32  $\mu\text{g}$  at the maximum position without the capillary array to 0.12  $\mu\text{g}$  with the capillary array. Since less molecules are evaporated to the sides, we were

able to use the molecules in the oven much more effectively. When integrating over the whole beam, the factor we gained by using the capillary array was 2-2.5.

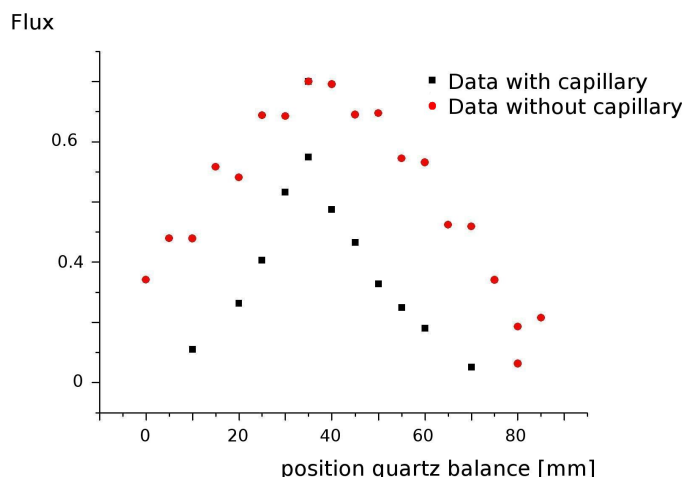


**Figure 2.9:** Flux measured for TPP. The temperature was kept constant during the measurement. The full width half maximum of the beam decreased by a factor of 2 when using the glass capillary array, hence, we could use the molecules more effectively. The transmission became lower by a factor 2-2.5.

The maximal flux for 335.5 °C is 9 ng/s, for the higher temperature 9.5 ng/s. The number of molecules per steradian per second can be determined by converting the flux from ng per second to molecules per second. The solid angle  $\Omega$  is calculated by

$$\Omega = \frac{A_q}{r^2} \quad (2.12)$$

where  $A_q$  is the surface of the quartz balance and  $r$  the distance from the oven orifice to the quartz balance.  $A_q$  was determined to be  $50 \cdot 10^{-6} \text{ m}^2$ , the distance  $r$  was 58.5 mm. The flux per steradian per second for the lower temperature was  $6.0 \cdot 10^{14}$  molecules, for the higher temperature  $6.4 \cdot 10^{14}$  molecules. Hence, at the higher temperature, the flux was 5 % higher.

After using the capillary array a couple of times it got blocked by the molecules. The reason for this was that the front of the oven was not heated properly and hence, the capillary array was at lower temperature.

Especially when using Rhodamine B which gets liquid as it is heated up the capillary could not be kept in front of the oven because it got stuck after just one heating cycle. For TPP the capillary array worked well for 2-3 heating circles, but eventually also was blocked by molecules.

## 2 Experimental setup

The flux of Rhodamine B was often very unstable due to the phase change from solid to liquid. The melting point of Rhodamine B is at 210 °C. The molecule starts decomposing at this temperature. The evaporation point is at 195-200 °C. During the heating often bubbles form inside the oven. Then the flux increased rapidly and the source emitted the molecules intermittently.

For TPP and Phthalocyanine the source worked well and we managed to get a constant flux. Care had to be taken of the pressure in the oven chamber. If the heating of the oven was started when the pressure was above  $5 \cdot 10^{-6}$  mbar, no molecular beam could be obtained. This was checked by measuring the profile of the beam. If the flux was distributed evenly in the x-direction, we had to reduce the temperature of the oven and wait for the pressure to decrease. Then another heating circle could be started.

The current source was already substituted by a laser evaporation source, where the molecules are evaporated by shining a laser onto them. The glass window the molecules are evaporated from can be covered with different molecules. Hence, it is possible to use different molecules without opening and refilling the oven. Furthermore, the heating load is reduced to a minimum because the laser is focused on a small spot of the glass window.

### 2.4 Detection surface

After passing the grating the molecules were deposited on a quartz surface in the detection chamber. The quartz plate is  $10 \times 10$  mm or  $25 \times 25$  mm big and about 170  $\mu\text{m}$  thick. It is glued to the aluminium plate, which is at the end of the detection chamber. Between the aluminium plate and the flange of the vacuum chamber a rubber ring was placed in order to keep the vacuum.

When gluing the quartz plate to the aluminium we had to take care of not using too much glue and tried to keep it as far away from the deposition surface as possible. Before attaching the aluminium plate to the vacuum chamber the glue had to dry thoroughly. Otherwise it got suck into the vacuum when opening the chamber to the prepumping system and the quartz surface was sputtered with glue.

The quartz plates used when illuminating the molecules from the inside of the vacuum chamber were coated like a dichroic mirror. The transmission curve of the slides for the green laser is shown in fig. 2.10. It can be seen that the green excitation laser light

is reflected and the red light at a wavelength above 580 nm transmitted. We also used coated quartz slides for the blue laser which worked in the same way. The main advantage was that the exciting laser light was prevented from entering the objective and thus, increasing the background signal. When illuminating the sample through the objective with the 660 nm laser the uncoated quartz slides were used.

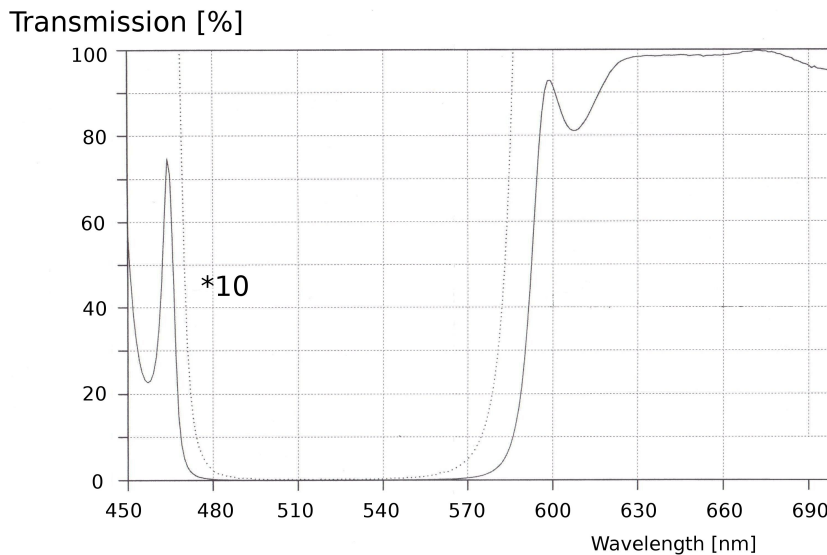


**Figure 2.10:** Transmission curve of the quartz slide with the coating for the green laser. The green excitation laser light is reflected, the molecules' fluorescence light transmitted. [33]

Not having a proper cleaned quartz slide of course increased the mean and complicated the detection of the interferograms. Hence, we thought of a possibility to attach the slides to the plate without gluing it. The solution was a coated quartz slide bonded to a glass plate (fig. 2.11) by diffusion bonding which was then attached to the vacuum chamber. The bonding was done by Laseroptik Garbsen. Diffusion bonding is accomplished without the need for a liquid interface or other joining processes such as melting or resolidification.

Diffusion bonding produces solid state coalescence between two materials. Joining occurs at a temperature below the melting point. Coalescence of contacting surfaces is produced with loads which are below those that would cause macroscopic deformation to the part. [34]

The transmission curve of the bonded glass is shown in fig. 2.12.

## 2 Experimental setup

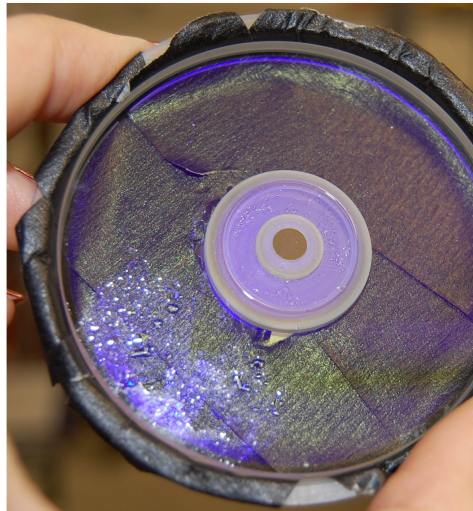


**Figure 2.11:** The round quartz slide in the middle is bonded to the glass plate by diffusion bonding.

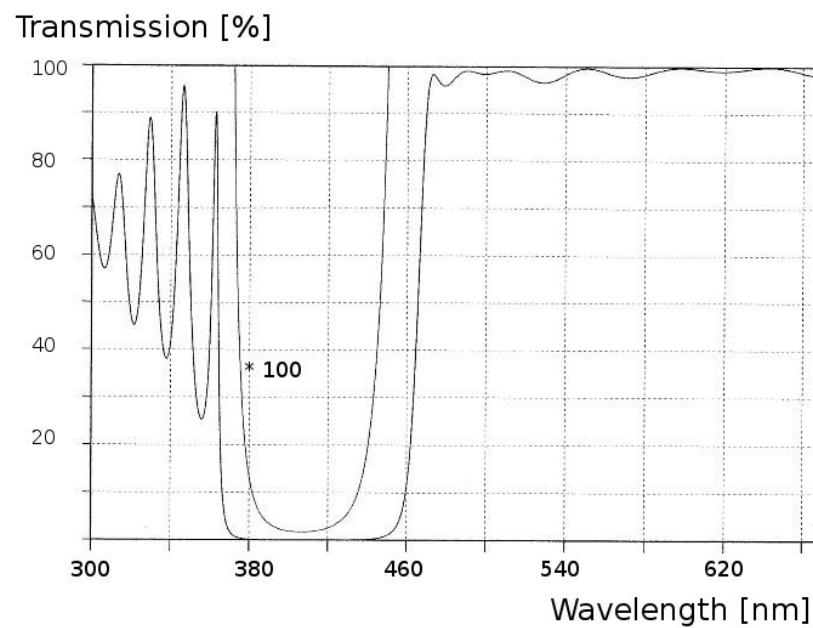


**Figure 2.12:** Here, the transmission curve for the bonded quartz is shown. It reflects wavelengths in the range of 380 to 400 nm and transmits the fluorescent light of the molecules. [33]



As deposition times, especially in the beginning of the interference experiments, often exceeded half an hour, we had to ensure that the drift of the quartz plate was within a negligible range. For 25 minutes we took images of the same section of the glass plate with a bright spot and kept track of the spot.

During this time window the drift of the quartz plate was  $0.2 \mu\text{m}$ , which is negligible for our measurements, since the distance between the interference maxima is in the range of 10 to  $20 \mu\text{m}$ .

## 2.5 Quartz balance

In order to control the flux from the oven, we used a quartz crystal microbalance (Inficon front load single crystal sensor). It measures the mass per unit area by measuring the change in frequency of a quartz crystal resonator. Since the quartz experiences the *piezoelectric effect*, one can apply alternating current to the crystal. This will induce oscillations, which are partially dependent on the thickness of the crystal. As mass is deposited on the surface of the crystal its thickness increases and hence, its frequency decreases. The *Sauerbrey equation* gives the correlation between the changes of the oscillations frequency and the mass deposited on a piezoelectric crystal [35]:

$$\Delta\nu = \frac{-2\Delta m\nu_0^2}{A\sqrt{\rho_q\mu_q}}\Delta m \quad (2.13)$$

where  $\nu_0$  is the resonant frequency,  $\Delta\nu$  is the frequency change,  $\Delta m$  is the mass change,  $A$  is the piezoelectrically active crystal area,  $\rho_q$  is the density of quartz ( $\rho_q=2.638 \text{ g/cm}^3$ ) and  $\mu_q$  is the *Shear modulus* of quartz for an AT-cut crystal ( $\mu_q=2.947\cdot 10^{11} \text{ g/cm}^2\text{s}^2$ ).

The equation is valid when the following three conditions are met: the deposited mass must be rigid, distributed evenly, and the frequency change  $\Delta\nu/\nu$  must be smaller than 2 %.

## 2.6 Gratings

### 2.6.1 Grating with 170 nm thickness

The silicon nitride grating fabricated by Tim Savas from MIT by photolithography [36] (fig. 2.13) is about 170 nm thick and has an opening fraction of 75 %. The opening

## 2 Experimental setup

fraction is defined as

$$f = \frac{\text{slit width}}{\text{grating constant}}. \quad (2.14)$$

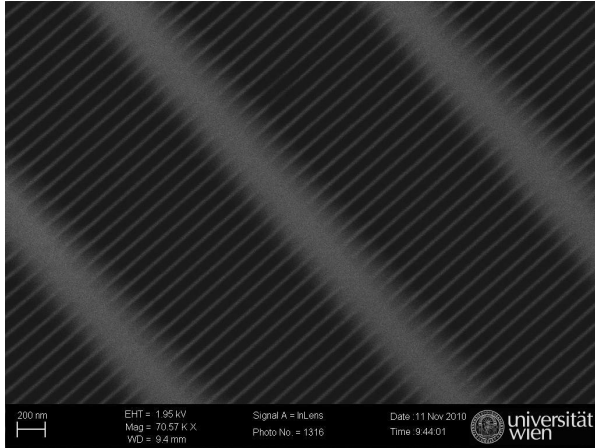


**Figure 2.13:** The grating shown here has an opening fraction of 0.75 and is 170 nm thick. The picture was taken in a scanning electron microscope. The grating constant is 100 nm, the lattice of the superseding structure is 1  $\mu\text{m}$  wide apart.

### 2.6.2 Gratings with 10 nm thickness

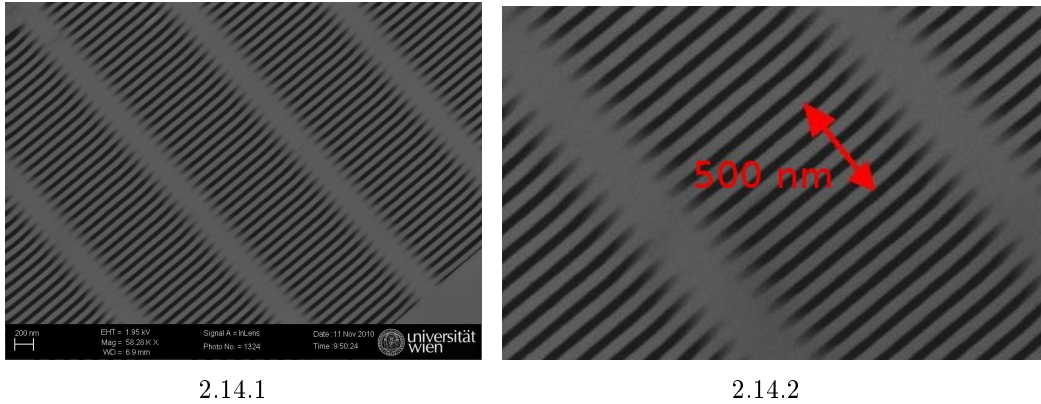
Thanks to the collaboration with Ori Chesnovsky and Alexander Tsukernik from the University of Tel Aviv, we were able to use much thinner gratings than those which were available before. As the thicker gratings they are also made of silicon nitride and are as thin as 10 nm. The technique used to fabricate the gratings is the *focused ion beam method* (FIB). FIB uses a finely focused beam of ions, usually gallium, and can be operated in low current mode for imaging and high current mode for sputtering and milling. The most fundamental difference between FIB and electron beam methods like SEM is the use of ions instead of electrons.

We used two 10 nm thick gratings with different opening fractions. One of them can be seen in figure 2.14.

The observation of interference on gratings of different thicknesses promises further interesting possibilities for investigation like the van der Waals interaction of the molecules with the grating.

The interactions occurring on thinner gratings made up of just a few atomic layers would probably be totally different from the interaction occurring between thicker gratings

and the molecules because the mass of the grating becomes comparable to the molecular mass.



2.14.1

2.14.2

**Figure 2.14:** Pictures taken in the scanning electron microscope from the 10 nm thick grating with an opening fraction of 0.5. The grating constant is 100 nm.

## 2.7 Electron multiplying CCD camera

The additional feature which makes the difference between a CCD camera and an EMCCD camera like the camera used in this experiment is that between the shift register and the output amplifier several multiplication registers are inserted.

In order to know how the intensity at the chip correlates to the photons per pixel, we had to calibrate the camera for different gains. First we calibrated the intensity of the light source, in our case a torch. We had two polarization filters. One was fixed, the other one rotatable. This way we could adjust the light intensity. Through the dichroic mirror just the red light reached the CCD chip. The green light was directed towards the Newport photodiode. The diode was placed in one straight line with the torch and the CCD chip. We measured the intensity for different diode positions and extrapolated the values for the position at which the CCD chip is.

Then the setup was changed as depicted in fig. 2.15.

The intensity of the light source was varied by rotating the filter. Then the intensities on the CCD chip and the diode were measured. The intensity per pixel per second on the CCD was then converted to photons per pixel per second. By multiplying this value by the intensity at the diode chip and dividing it by the intensity at a certain

## 2 Experimental setup

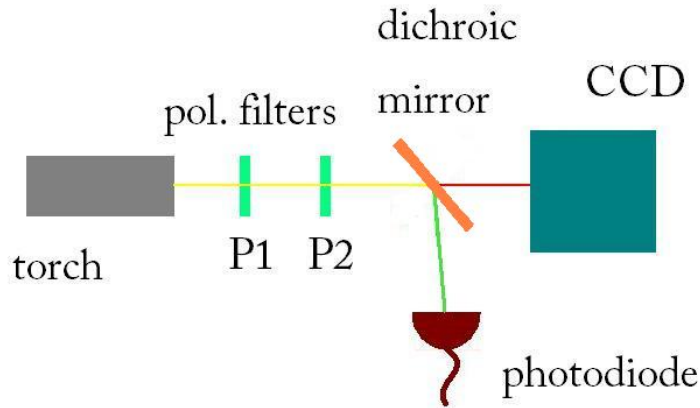


**Figure 2.15:** Calibration setup for the EMCCD camera. P1 is the rotatable polarization filter, P2 is fixed. The intensity was varied by rotating the filter and measured on the CCD chip and the diode.

position of the polarization filter the intensity measured on the chip is independent from fluctuations in the light source.

The intensity on the CCD chip can be calculated as follows:

$$I = \frac{\text{Photons} \cdot \text{ND} \cdot I_{\text{Diode}}}{\text{px} \cdot \text{s} \cdot 56.6 \times 10^{-6} \text{W}} \quad (2.15)$$

All measurements were done with a ND 6 and ND 4 filter.

After knowing which intensity corresponds to which number of photons per pixel, we measured the counts for gain 110, 130 and 150 for two different pre-amplifier gain settings. (fig. 2.16 and 2.17).

In the figures it can be seen that there is a linear correlation between the counts and the photons per pixel. Just when the intensity gets very low ( $<1$  photon per pixel), deviations from the linearity can be obtained.

The measurements were carried out for two different pre-amplifier gain settings. An EMCCD sensor can have a much larger dynamic range than can be reproduced with the Analogue/Digital converters currently available on the market. To access the range of signals it is necessary to allow different pre-amplifier gain settings. A higher setting means fewer electrons per count, resulting in a lower system noise floor and therefore a higher SNR versus dynamic range. However, high settings may not match well to the pixel well depth of the sensor. Therefore, a lower setting can be selected to meet the full well depth potential. [37]

$\alpha$ [°]	I [ $\mu$ W]	$I_{\text{extrapol.}}$ [ $\mu$ W]	$I_{\text{CCD}}$ [ $\mu$ W/px/sec.]	ph/px/sec. on CCD
0	26.5	25.7	$1.6 \cdot 10^{-5}$	$5.3 \cdot 10^7$
10	25.0	24.3	$1.6 \cdot 10^{-5}$	$5.01 \cdot 10^7$
20	22.0	21.4	$1.4 \cdot 10^{-5}$	$4.41 \cdot 10^7$
30	18.2	17.7	$1.1 \cdot 10^{-5}$	$3.65 \cdot 10^7$
40	13.9	13.5	$8.6 \cdot 10^{-6}$	$2.79 \cdot 10^7$
50	9.1	8.8	$5.6 \cdot 10^{-6}$	$1.82 \cdot 10^7$
60	4.7	4.6	$2.9 \cdot 10^{-6}$	$9.48 \cdot 10^6$
70	1.7	1.6	$1.0 \cdot 10^{-6}$	$3.35 \cdot 10^6$
80	0.2	0.2	$1.4 \cdot 10^{-7}$	$4.41 \cdot 10^5$
90	0.9	0.9	$5.7 \cdot 10^{-7}$	$1.83 \cdot 10^6$
Diode at diode pos.	$\alpha=70$			
70	$56.6 \mu\text{W}$			

**Table 2.1:** The photons had a wavelength of approximately 641 nm. The area of the CCD chip was  $0.64 \text{ cm}^2$  and the area of the diode chip was  $1 \text{ cm}^2$ . The intensity was varied by rotating the polarization filter and the intensity measured on the diode extrapolated to the intensity on the CCD chip. The obtained intensity was converted into photons per pixel per second.

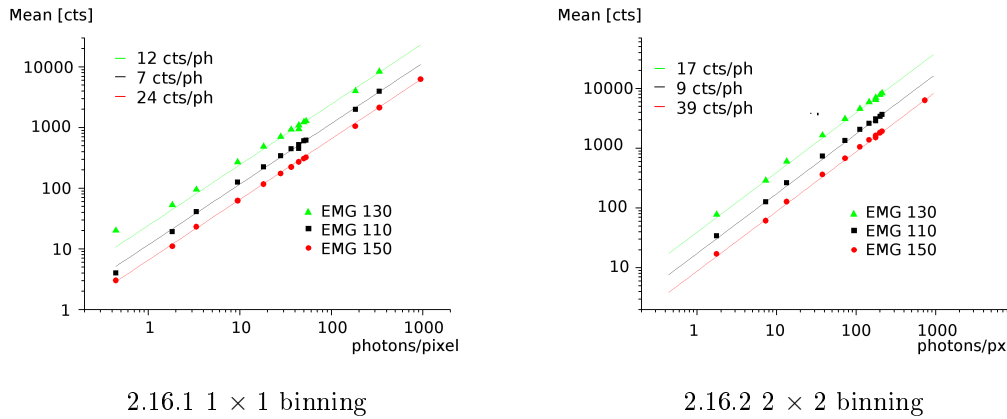


**Figure 2.16:** Calibration curves for a pre-amplifier gain setting of 4.1. We measured the counts of our EMCCD for different intensities (hence, photons per pixel) with three gain settings which were usually used during the experiment. There is a linear correlation between the counts and the intensity, except for very low count rates (less than one photon per pixel).

It was observed that when the pre-amplifier gain is set to 4.1 instead of 2.0, the EMCCD is  $1.90 \pm 0.01$  times more sensitive. In the specification sheet of the EMCCD a value of 2.01 was obtained.

## 2 Experimental setup

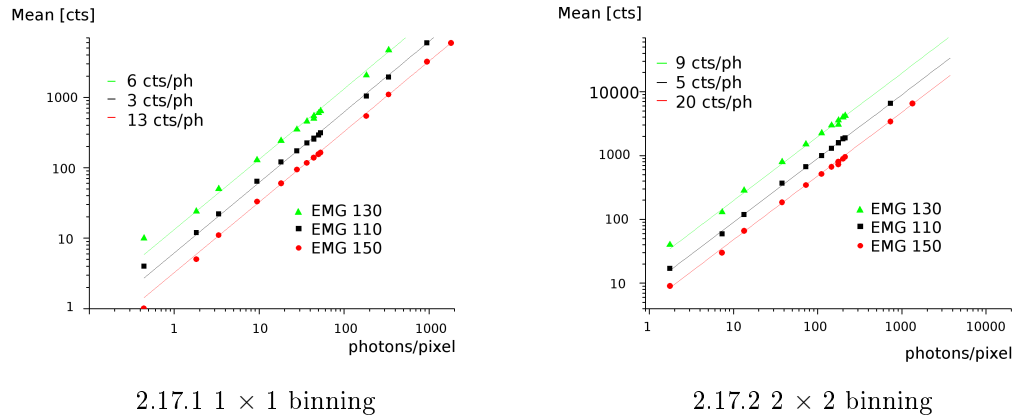


**Figure 2.17:** Calibration curves for a pre-amplifier gain setting of 2.0. The EMCCD counts were measured for different intensities (hence, photons per pixel) with three gain settings which were usually used during the experiment. There is a linear correlation between the counts and the intensity, except for very low intensities (less than one photon per pixel). The counts for this pre-amplifier gain setting were lower than for the setting applied in fig. 2.16.

The output of the gain register is fed into a CCD output amplifier. This amplifier will have a readout noise around 10 to 20 electrons at MHz readout rates. This noise will be effectively reduced by the multiplication factor of the gain register. So, by using the gain one can reduce the noise to insignificant levels at any readout speed. At the same time one adds some noise to the measured signal due to the statistical nature of the multiplication process.

At high gain the noise is calculated as the square root of the signal  $N$  (number of electrons). This will add to the shot noise of the signal to become  $\sqrt{2N}$ . If the signal is large enough to be above the readout noise then there is probably no need for applying an EMGain. If the signal is lost in the readout noise, then increasing the gain is the only way to detect it.

The EMCCD calibration was expanded to all EMGains. The objective was moved away from the glass surface a few millimeters. In this way, some of the ambient light could reach the chip of the camera. We did not use the laser as the light source because we wanted to make sure that no bleaching occurs during the measurement. The mean of a central spot of the field of view was measured. It increased logarithmically with the EMGain. The background was subtracted after the measurement. As can be seen in fig.

Readout rate [MHz], binning	A	B
35, 1 × 1 (a)	1.3	0.0153
35, 1 × 1 (b)	1.3	0.0154
35, 2 × 2	2.2	0.0130
13, 1 × 1	1.0	0.0149
13, 2 × 2	2.0	0.0128

**Table 2.2:** Coefficients for the fit  $\log(\text{mean}) = A + B \cdot \text{EMGain}$ . The slope for the different readout rate and binning settings hardly varies.

2.18, the curves look similar for high count rates. The red and black curves show that the measurement is reproducible. The other curves were done at different readout rates (13MHz or 35MHz) and different binning ( $1 \times 1$  or  $2 \times 2$ ).

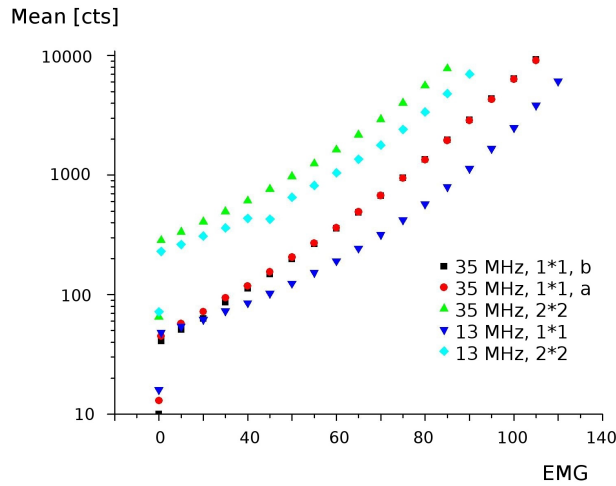


**Figure 2.18:** Here, the calibration curves as a function of the EMGain for different readout rates and binnings are shown. For high count rates the curves look similar.

We did a linear fit for the measured curves for a EMGain between 90 and 150. The slope hardly varies for the different settings (see table 2.2).

## 2.8 Lasers

All lasers used in this experiment were CW lasers. For the illumination at 532 nm we used a solid state laser diode bought from Roithner Lasertechnik (RLTMGL-532-100). The

## 2 Experimental setup

power was tunable from 0-100 mW. The other lasers used are specified in the following two sections.

### 2.8.1 660 nm laser

We used the ML101J27 Mitsubishi Laser Diode which we connected to the LDC205C Benchtop LD Current Controller. The power was tuneable from 1 to approximately 100 mW. The illumination scheme for the 660 nm laser differed from the one for the green and the blue laser, because we were lacking the coated slides for the red laser. Therefore, the sample was illuminated through the objective by placing a dichroic mirror behind it which reflects the red light at 660 nm and transmits the fluorescence light above 680 nm (fig. 2.19). So, the scheme here was equal to epifluorescence illumination, where the sample is illuminated through the objective. The red light causes much less autofluorescence in the objective and the glass. Furthermore, the extinction coefficient of Phthalocyanine was higher at 660 nm than the extinction coefficient of TPP at 532 nm.

Two excitation filters (Brightline HC 655/49, F39-655) were used in order to avoid that ambient light enters the optical path. There were three emission filters (Brightline HC 736/128, F37-738) between the dichroic mirror and the EMCCD camera to ensure that just light which has a wavelength according to the emission wavelength of Phthalocyanine arrives at the CCD chip.

### 2.8.2 445 nm laser

For excitation at a wavelength of 445 nm we used the Spyder III Pro Arctic Series bought from Wicked Lasers. Since the laser was lacking a proper specification sheet, we had to measure its polarization, exact power, emitted wavelength and whether the power stays constant. The spectrum of the laser is shown in fig. 2.20.

The polarization of the laser was measured for the high and the low energy mode. In the low energy mode the emitted power is about 48 mW, in the high energy mode about 100 mW. In fig. 2.21 the polarization measured for the two energy modes is shown.

In order to see whether the power stays constant when the laser is switched on over a longer period of time, the output was measured by a powermeter for about 35 minutes. Within that time, the power stayed stable enough for our purposes. It dropped from 50



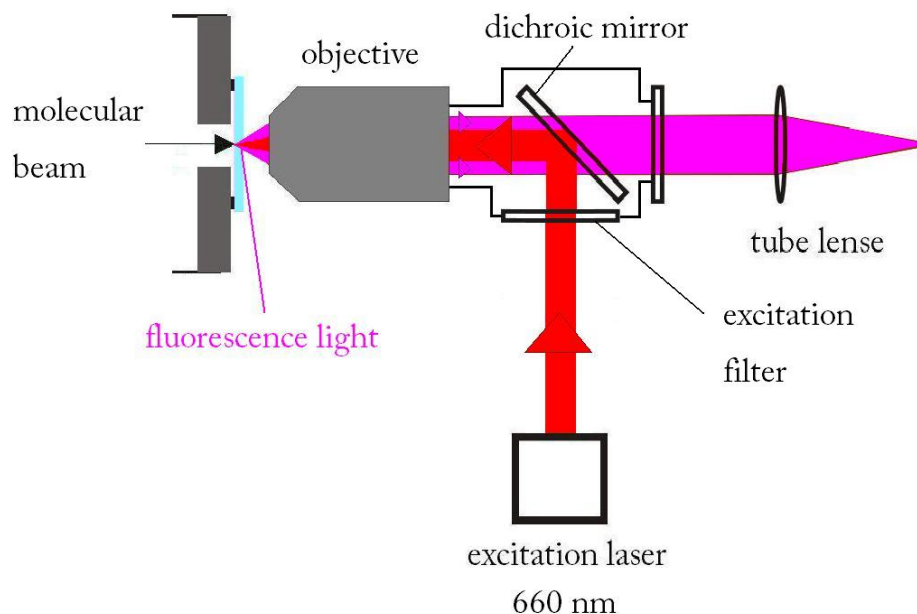


**Figure 2.19:** The molecules deposited on the quartz slide were illuminated through the objective. Due to the low autofluorescence of the filters and the slide at 660 nm the background light could be kept low. The ambient light was blocked by an excitation filter which transmitted just the excitation laser light. The dichroic mirror reflected the laser light towards the molecules, they were excited at the glass slide and emitted fluorescence light, which passed through the dichroic mirror and reached the EMCCD camera through the tube lens and an emission filter.

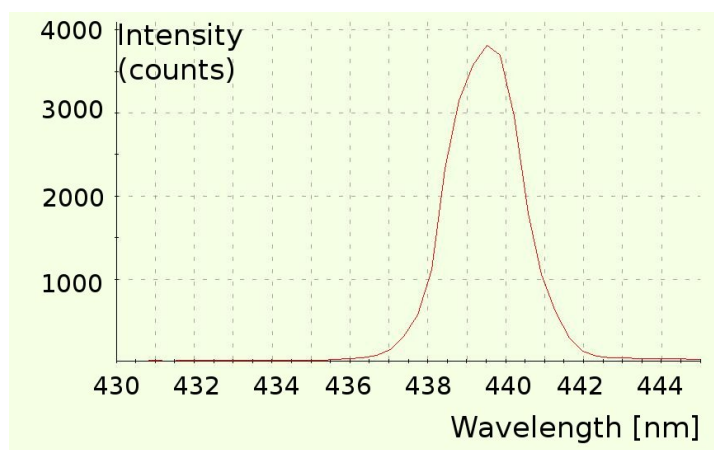


**Figure 2.20:** Spectrum measured for the 445 nm laser.

to 48 mW in the first 5 minutes and then stayed constant.

## 2 Experimental setup

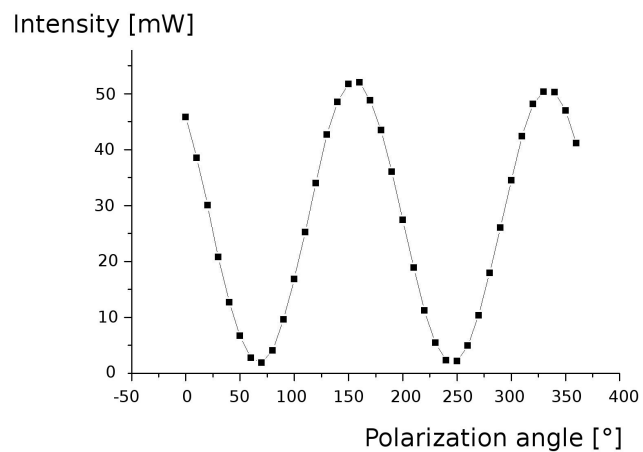


**Figure 2.21:** Polarization of the 445 nm laser: It can be seen that the laser is completely polarized as the power goes to zero for certain polarization angles.

The excitation filter used for this laser was the laser clean-up filter z 532/10. In contrast to the green and the red laser, the blue laser causes much more bleaching.

# 3 Fluorescence

## 3.1 Fluorescence mechanism

Luminescence occurs when a substance absorbs and then emits light of a different wavelength. In most cases the emitted light has a longer wavelength and thus, lower energy due to the *Stokes Shift*. Fluorescence is a special case of luminescence. In excited singlet states the spin of the excited electron is the opposite to the spin of the electron paired to the excited one. Therefore, the return to the ground state is spin allowed and occurs rapidly by emission of a photon. The typical lifetime of a fluorophore, which is the average time in between the excitation and the return to the ground state, is about 10 ns. In order to achieve a deeper understanding of how fluorescence works, a so-called *Jablonski diagram* should be considered (fig. 3.1).

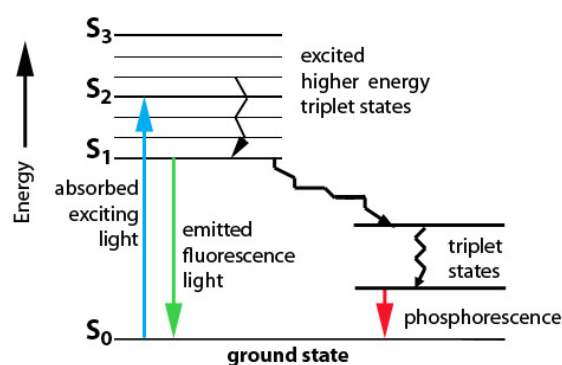


**Figure 3.1:** The diagram shows a number of possible routes by which an excited molecule can return to its ground state. A rapid return is known as fluorescence, a delayed one, ie. via triplet states, as phosphorescence. [38]

## 3.2 Quantum yield

To have an idea about how efficient the process of fluorescence for a particular fluorophore is, one has to consider the quantum yield  $\Phi$ . It is defined as the number of photons emitted divided by the number of photons absorbed.

$$\Phi = \frac{\# \text{ emitted photons}}{\# \text{ absorbed photons}} \quad (3.1)$$

It is given by

$$\frac{\Gamma}{\Gamma + \kappa_{nr}} \quad (3.2)$$

The radiationless decay rate  $\kappa_{nr}$  and the rate of radiative decay  $\Gamma$  both depopulate the excited state population.

## 3.3 Fluorescence lifetime

By the lifetime the average time the molecule stays in the excited state before emitting a photon is measured. Assume a fluorescence sample is excited with an infinitely sharp pulse of light. This results in an excited-state population  $n_0$  which decays with a rate  $\Gamma + \kappa_{nr}$  according to

$$\frac{dn(t)}{dt} = -(\Gamma + \kappa_{nr})n(t) \quad (3.3)$$

$n(t)$  is the number of excited molecules at time  $t$  following excitation,  $\Gamma$  is the emissive rate and  $\kappa_{nr}$  is the non-radiative decay rate. Since emission of a photon is a random event and each fluorophore has the same probability of emitting a photon at a given period of time, the excited state population decays exponentially. Written in terms of the time-dependent intensity  $I(t)$  we get the following expression

$$I(t) = I_0 \cdot e^{-t/\tau} \quad (3.4)$$

where  $I_0$  is the intensity at time 0. The lifetime is the inverse of the total decay rate. It is the average amount of time a fluorophore remains in the excited state  $\langle t \rangle$

following excitation. This can be calculated by averaging  $t$  over the intensity decay of the fluorophore:

$$\frac{\int_0^{\infty} tI(t)dt}{\int_0^{\infty} I(t)dt} = \frac{\int_0^{\infty} te^{-t/\tau} dt}{\int_0^{\infty} e^{-t/\tau} dt} \quad (3.5)$$

After integration one finds out that the denominator is equal to  $\tau$  and the numerator to  $\tau^2$ . This means, that for a single exponential decay the average time a fluorophore stays in the excited state is equal to the lifetime

$$\langle t \rangle = \tau. \quad (3.6)$$

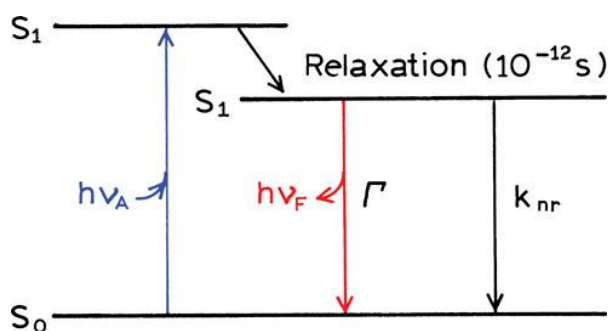


**Figure 3.2:** Illustration of the meaning of the lifetime and the quantum yield of a fluorophore. The quantum yield of the fluorophore illustrated is given by  $Q = \Gamma/(\Gamma + \kappa_{nr})$  and the lifetime by  $\tau = 1/(\Gamma + \kappa_{nr})$ . [39]

The lifetime of a fluorophore in the absence of non-radiative processes is called the intrinsic or natural lifetime. It is given by

$$\tau_n = \frac{1}{\Gamma} \quad (3.7)$$

The *extinction coefficient* is a measurement of how strong a substance absorbs light at a given wavelength. It can whether be given per unit mass or per mole.

## 3.4 Fluorescence quenching

Several processes can be involved in the decrease of the intensity of fluorescence, the so-called *fluorescence quenching*. There is for example collisional quenching, as shown in the Jablonski diagram in figure 3.3. The fluorophore is returned to the ground state during a diffusive encounter with a quencher. There are a lot of molecules which can act

### 3 Fluorescence

as quenchers, as oxygen, halogens, amines and electron-deficient molecules.

Apart from collisional quenching, there are a lot of other mechanisms which lead to fluorescence quenching. Fluorophores can form nonfluorescent complexes with quenchers, the intensity of the fluorescence can be attenuated by the fluorophore itself or other absorbing molecules.

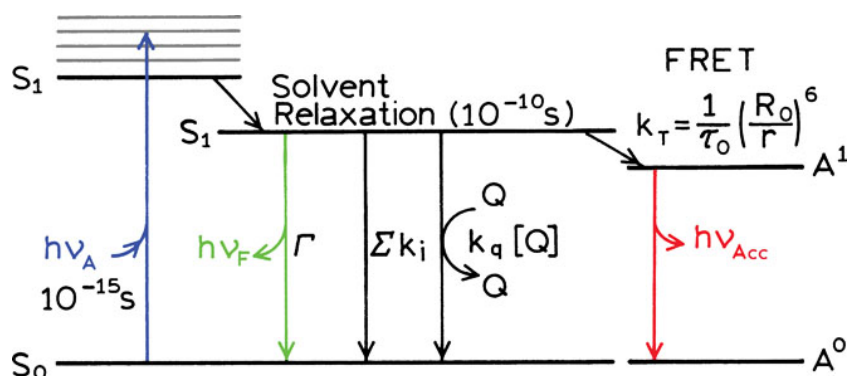


**Figure 3.3:** Jablonski diagram with collisional quenching and fluorescence resonance energy transfer. The fluorophore is returned to the ground state during a diffusive encounter with a quencher. The decrease in intensity is described by the Stern-Volmer equation.  $\kappa_q$  is the biomolecular quenching constant,  $\tau_0$  the unquenched lifetime and  $[Q]$  is the quencher concentration.  $\Sigma k_i$  indicates non-radiative paths to the ground state. [40]

### 3.5 Bleaching and blinking

*Photobleaching* is the photochemical destruction of a fluorophore. It occurs when a fluorophore loses the ability to fluoresce due to photon-induced chemical damage and covalent modification [41]. The number of excitation and emission cycles that occur for a particular molecule before photobleaching is dependent on the molecular structure and the environment. Very often the photobleaching also includes photodynamical processes, meaning they involve the interaction of the fluorophore with oxygen. The photostability of a fluorophore is given by its photobleaching quantum yield  $\Phi_B$  or its inverse  $\mu = 1/\Phi_B$ .  $\mu$  is the average number of cycles a fluorophore can undergo before photobleaching.

To get the average number of photons emitted by a fluorophore during its whole lifetime, we have to multiply  $\mu$  by the quantum yield. The number of cycles for a good

fluorophore as i.e. Rhodamine 123 is 1.600.000 [41]. Of course, this number varies widely depending upon the conditions of the sample.

Each fluorophore displays blinking when illuminated with high intensities. Blinking can be described as a dramatic fluctuation in intensity. The main reason for blinking is believed to be intersystem crossing (ISC) to the triplet state. ISC is a radiationless transition from an excited state into another with different spin multiplicity. (fig. 3.4)

If an electron in a molecule or atom is excited, then either an excited singlet or excited triplet state will form. The singlet state is such a state that the spin of the excited electron is still paired with the spin of the ground state electron. In triplet states the electron is no longer paired with the ground state electron. Since this is a spin forbidden transition, it is more likely that the transition to the singlet state forms.

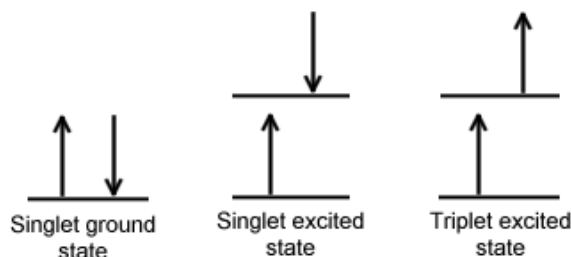


**Figure 3.4:** In a singlet state all electron spins are paired. Hence, the spin of the excited electron is still paired with the ground state electron. In a triplet state the electron spins are not paired and hence, they are parallel. Since excitation to the triplet state requires a forbidden spin transition it is more probable that a singlet excited state forms. [42]

In principle, the spin of the electron is reversed. The more the two vibrational levels of the excited states overlap, the more probable it is that this process occurs. The process can be understood from the kinetic equations for the population of the S state. The number of molecules in the first singlet state is given by

$$S_1 = \frac{\tau\sigma I_e S_T}{1 + I_e/I_s} \quad (3.8)$$

The excitation rate is proportional to the excitation intensity  $I_e$  and the cross-section for the absorption  $\sigma$ .  $S_T$  is the total number of fluorophores and  $\tau$  is the lifetime.

### 3 Fluorescence

Good fluorophores such as Rhodamine can emit  $10^5$  to  $10^6$  photons prior to destruction. The interaction with oxygen has two interesting effects. It can react with the excited states and destroy the fluorophore. But when quenching the  $T_1$  state, the  $T_1$  population is decreased and the molecule can return faster to the ground state. In fact, brighter single molecule emission in an oxygen environment was observed relative to an oxygen-free sample.



# 4 Molecules

## 4.1 Tetraphenylporphyrine- TPP

TPP is a natural dye molecule with a molar mass of 614.7 amu. Its structure is given in fig. 4.2. It is of high importance in medical and biological sciences, since it exists in animals and plants and is also involved in the process of photosynthesis. There is a great number of articles existing about the characterization of TPP [43, 44]. TPP was the first biomolecule where matter wave interference was shown with the Talbot-Lau interferometer [45].

The excitation and emission spectra are shown in fig. 4.1.

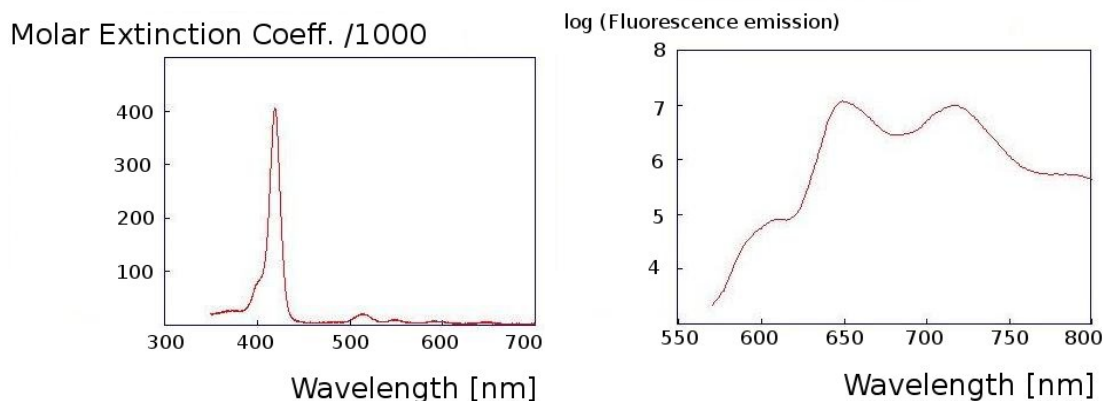


**Figure 4.1:** TPP excitation and emission spectra. The excitation maximum is at around 425 nm, another local maximum is at 530 nm. [46]

The quantum yield was determined to be 0.11 [47]. The molar extinction coefficient for TPP dissolved in toluene is about  $4 \times 10^5 \text{ Mol}^{-1} \text{ cm}^{-1}$  for an excitation wavelength of 420 nm [48], which is fairly high compared to other fluorophores.

The TPP we used in our experiment was bought from *Sigma Aldrich*.

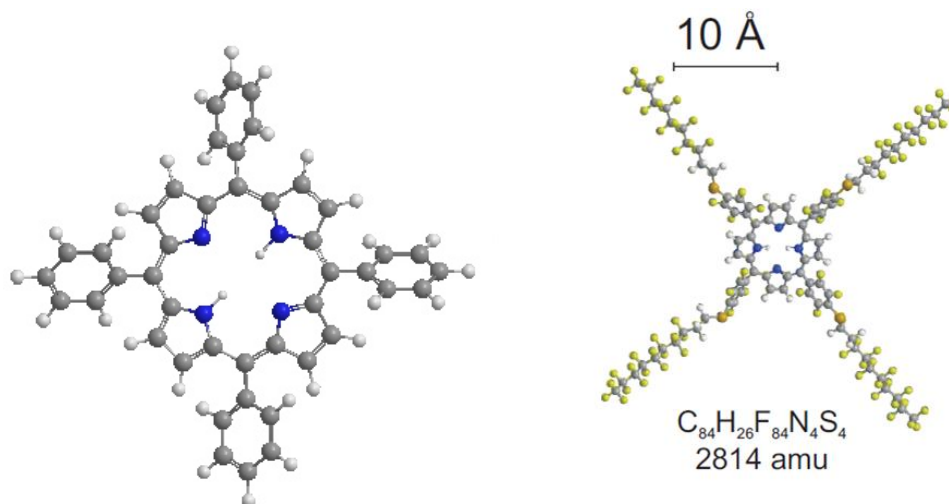


**Figure 4.2:** TPP has a mass of 614.7 amu. The first matter wave interference with biomolecules was shown with TPP. The atomic mass of TPPF<sub>84</sub> is 2814 amu. In diameter the molecule is over 30 Angstroem.

#### 4.1.1 TPPF<sub>84</sub>

Porphyrins show for our purposes convenient properties. They do not degenerate after the evaporation process and have a quite high vapor pressure. Therefore, they were functionalized by attaching fluor chains to the central ring (see fig. 4.2). The porphyrine derivatives we use were functionalized by the group around Marcel Mayor at the university of Basel.

Since the absorption spectra of TPPF<sub>84</sub> are not known yet, we measured them in a Perkin Elmer spectrometer. The molecule was dissolved and dropped on a glass slide. After drying the glass slide was placed in the spectrometer. Since in some areas of the slide the molecules clustered together and in others they did not, we took several measurements from the different areas. For comparison, TPP was dissolved and dropped on the slide in order to compare the spectrum of it with the spectrum of the heavier molecule (fig. 4.3).

When observing fig. 4.3, it can be seen that the maximum for clusters at approximately 510 nm is not as high as for not clustered TPPF<sub>84</sub>. Furthermore, the absorption wavelength for TPP is about 5 nm red-shifted in comparison to the TPPF<sub>84</sub>.

The spectrum measurements were just done qualitatively in order to make sure that

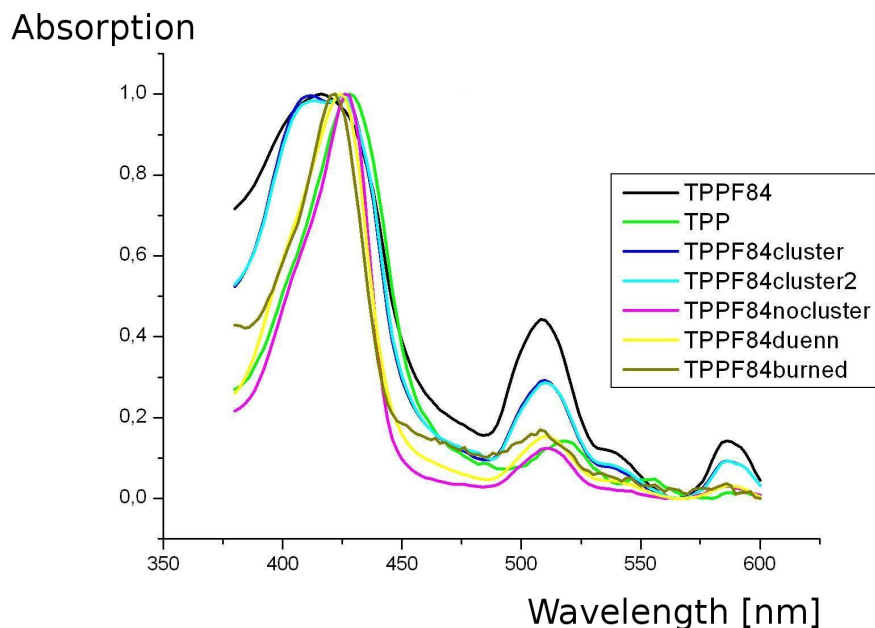


**Figure 4.3:** Absorption spectra for TPPF<sub>84</sub>. All spectra are normalized to the range 0-1. The maximum for clusters at approximately 510 nm is not as high as for not clustered TPPF<sub>84</sub>. For TPP the absorption wavelength is about 5 nm red-shifted in comparison to the TPPF<sub>84</sub>.

the spectra do not look completely different. Since the spectra did not show significant differences, we did not undertake further measurements.

## 4.2 Rhodamine B

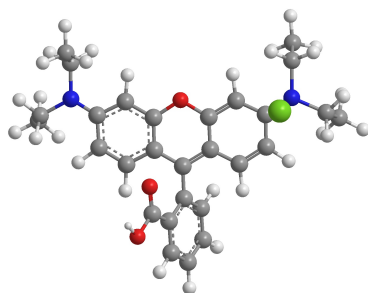


**Figure 4.4:** Structure of Rhodamine B. The molecule's mass is 479 amu, its structure formula  $C_{28}H_{31}ClN_2O_3$ .

Rhodamine B (fig. 4.4) is a dye molecule with a molar mass of 479 amu. Its chemical formula is  $C_{28}H_{31}ClN_2O_3$ , it was bought from *Sigma Aldrich*. The excitation

## 4 Molecules

and emission spectra are shown in fig. 4.5.

The quantum yield of Rhodamine B in basic ethanol is 0.7. [49]

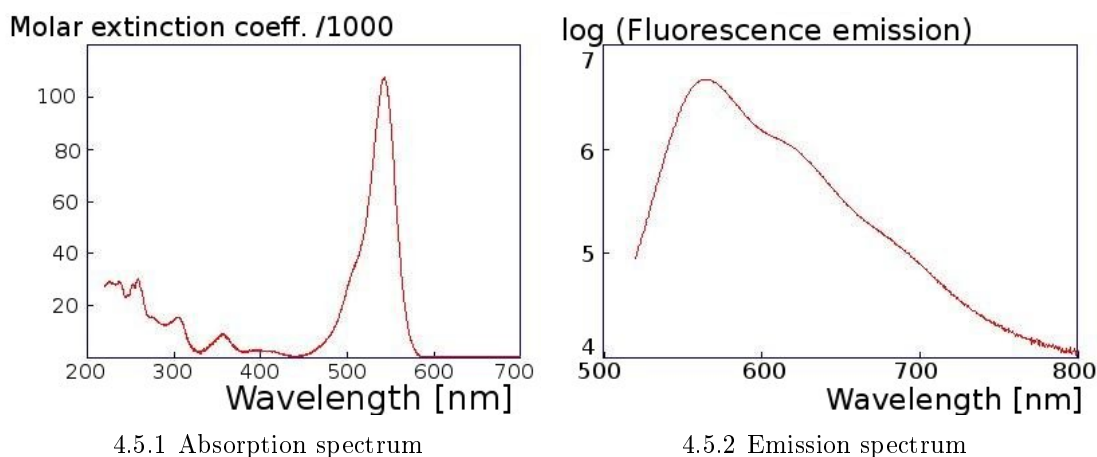


**Figure 4.5:** Excitation and emission spectra of Rhodamine B. The excitation maximum is at around 550 nm. [46]

It is the best fluorophore used in our experiments considering the excitation coefficient and quantum yield.

## 4.3 Phthalocyanine

Phthalocyanine is a dye molecule as TPP and Rhodamine B. Its structure can be seen in fig. 4.6. It has a molar mass of 514.5 amu and with  $162000 \text{ Mol}^{-1}\text{cm}^{-1}$  at 698.5 nm [46] a higher excitation coefficient than TPP. The quantum yield is 0.6, almost as high as of Rhodamine B. The molecular formula of Phthalocyanine is  $\text{C}_{32}\text{H}_{18}\text{N}_8$ .

The excitation and emission spectra are shown in figure 4.7.

The spectra were always measured for the molecule dissolved in a solution. Therefore, the spectrum for phthalocyanine was measured by ourselves. First, the molecule was dissolved in water and then dried out on a glass plate. This method did not work well, because the spectrum always turned out to be oversaturated. By simply rubbing the powder on a glass plate, the spectra were less saturated and it can be seen that the shape of the curves is approximately the same. Also the absorption of the molecule is at its maximum at the same wavelength for both spectra, shown in fig. 4.8.

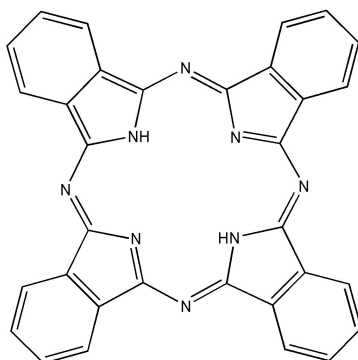
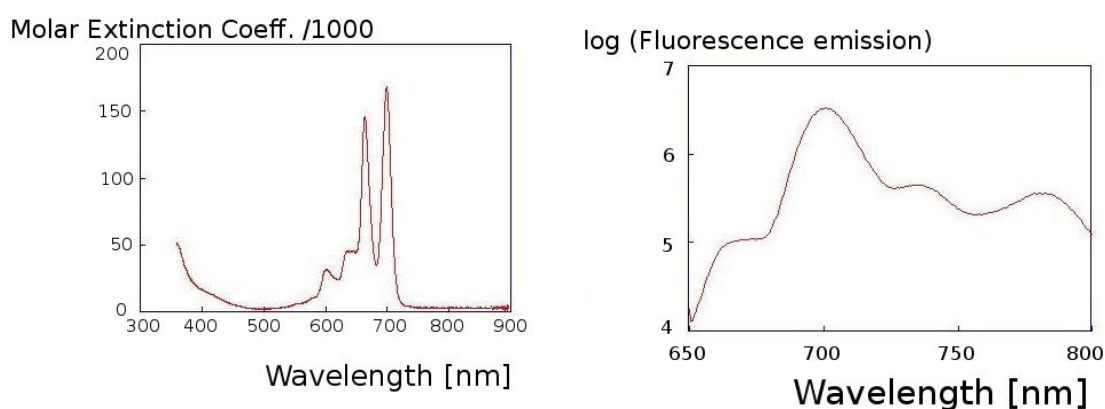


**Figure 4.6:** In this picture the structure of Phthalocyanine is shown [50]. Its molecular formula is  $C_{32}H_{18}N_8$ . Due to the high extinction coefficient and the molecule's absorption maximum at wavelengths above 650 nm it was very convenient using this molecule for single molecule detection.



4.7.1 Absorption spectrum

4.7.2 Emission spectrum

**Figure 4.7:** Excitation and emission spectra of Phthalocyanine. There are two excitation maxima, both between 650 and 720 nm. [46]

Furthermore, the enthalpy of vaporization of phthalocyanine was measured. The temperature of the oven was increased step by step and the amount of molecules accumulating on the quartz balance and the pressure were measured.

For small changes in temperature we can consider the enthalpy of vaporization of a substance as constant. Then, the vapor pressure and the temperature obey the following form of the Clausius-Clapeyron equation:

$$\ln p = -\frac{\Delta H}{RT} + C_1 \quad (4.1)$$

From the equation for ideal gases we get  $p = mRT/MV$ , where  $m$  is the mass in grams,

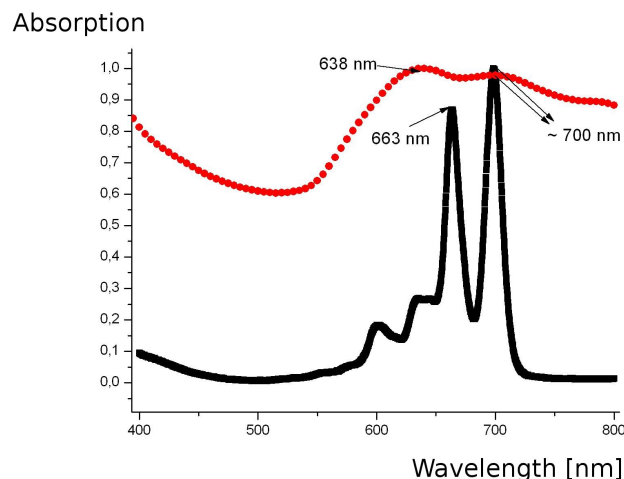


**Figure 4.8:** The red dots indicate the absorption spectrum for phthalocyanine rubbed on the glass plate, the black ones the spectrum for in chloronaphthalene dissolved phthalocyanine. Although the spectrum measured by ourselves was oversaturated, we could tell that the absorption wavelength is approximately the same for both samples.

$R=8.314$  J/mol/K the universal gas constant,  $T$  the temperature in Kelvin,  $M$  the molar mass in amu and  $V$  the volume in  $\text{dm}^3$ . When replacing  $p$  in the Clausius Clapeyron equation with this expression for the ideal gas, the universal gas constant  $R$ , the temperature, the molar mass and the volume can be taken out of the logarithm since they are constant values and the equation looks as follows:

$$\ln m \cdot T = \frac{\Delta H}{RT} + C_2 \quad (4.2)$$

From here we can calculate the enthalpy. Only the values measured from a temperature of 667 K to 719 K were considered because at lower temperatures the flux measured with the quartz balance was too low.

In fig. 4.9 the linear fit is given. From the slope the enthalpy of vaporization can be calculated. It was determined to be 194.9 kJ/mol.

## 4.4 Velocity and mass spectra

Due to the setup the velocities of the molecules we used could not be measured during the experiment itself. Therefore, we attached our source to a Time of Flight spectrometer (TOF) and measured the velocity distribution for the different molecules.

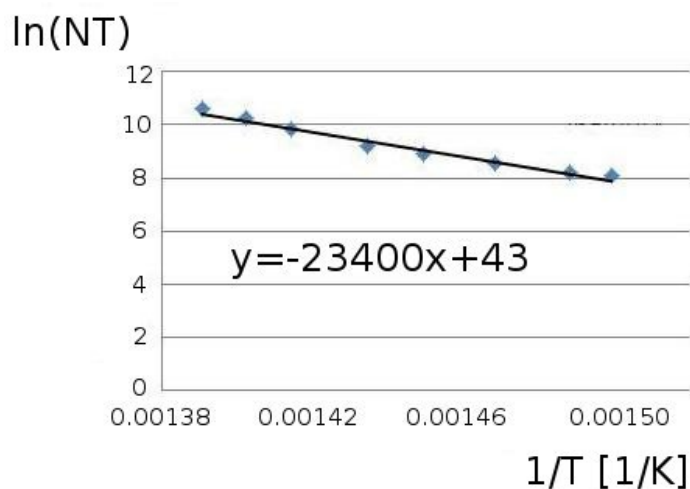


**Figure 4.9:** From the slope the enthalpy of vaporization for Phthalocyanine was calculated.

In the TOF a chopper divides the beam into bunches and the arrival times are measured in a quadrupole mass spectrometer. The measured time distribution needs to be deconvoluted from the chopper function in order to get the true velocities.

In fig. 4.10 the deconvoluted time distributions of TPP and Rhodamine B are shown. We did the measurements for slightly different temperatures since we wanted to check whether the molecular beam gets supersonic. Measurements were also done for even higher temperatures, but except the molecule decomposing we could not see any significant changes considering the particle velocity. From those time distributions we calculated the mean velocities for the molecules.

A gaussian curve was fitted to the data points measured in the TOF and the maximum was picked. The distance from the chopper to the QMS was 0.85 m.

For TPP the mean velocity was determined to be  $v_{\text{mean}} = 0.85 \text{ m} / 0.0045 \text{ s} = 187 \text{ m/s}$ . For Rhodamine B we calculated the same mean velocity.

The De Broglie wavelength for the molecules was determined to be  $\lambda_{\text{TPP}} = 3.45 \text{ pm}$  for TPP and  $\lambda_{\text{RhoB}} = 3.45 \text{ pm}$  for Rhodamine B.

The mass spectra were measured to check whether the molecules decompose in our source. We were especially interested in the mass spectra of Rhodamine B because the distances of the maxima measured did not match with the distances expected, as

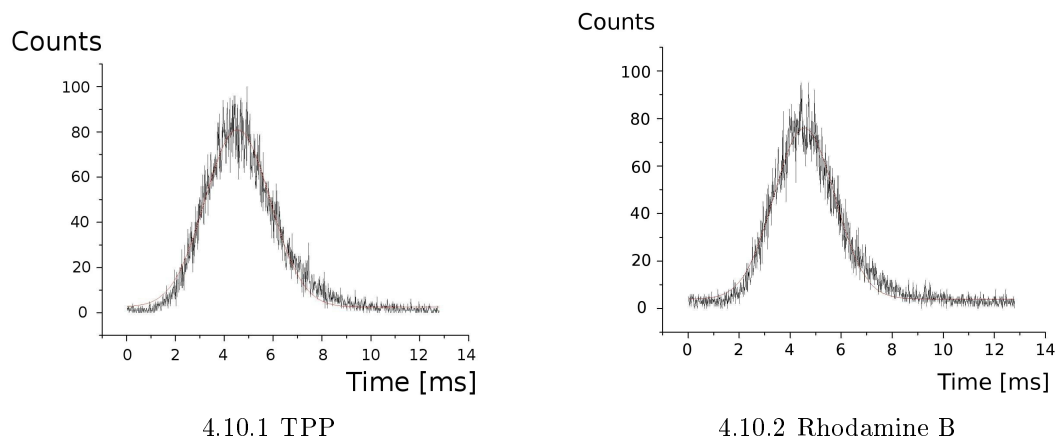


**Figure 4.10:** Deconvoluted distributions of TPP and Rhodamine B for different temperatures measured in the TOF.

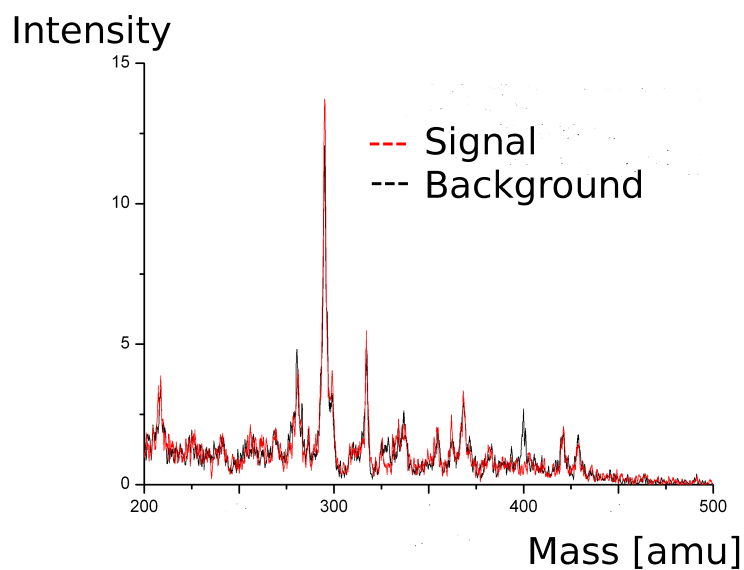
discussed later in section 6.

In fig. 4.11 the mass spectra measured at two different temperatures are shown. A small peak at 400 amu can be seen after heating the source up to 192 °C in the upper picture of fig. 4.11. After reaching a temperature of 212 °C a second peak at 328 amu shows up (bottom picture in fig. 4.11).

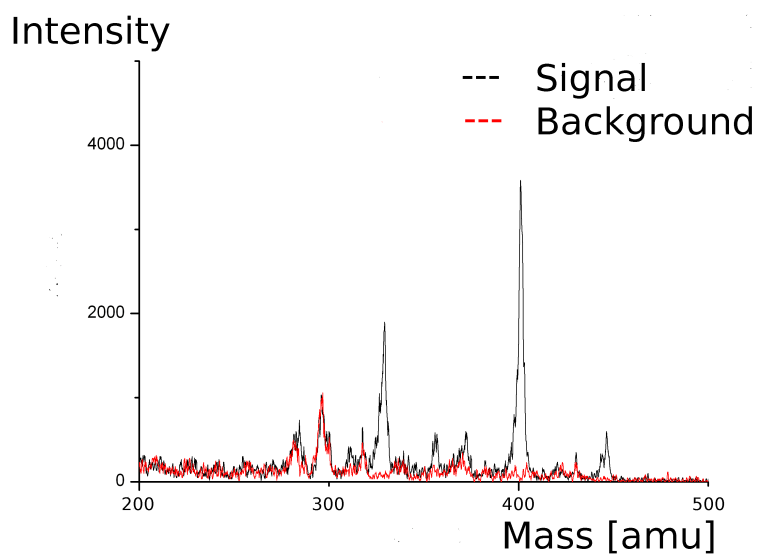
Since the measured distances of the maxima were too small for the mass of Rhodamine B, we expected to see a higher mass in the mass spectrum. We expected that Rhodamine B clusters form in the source and due to that we get the smaller separation in the interferogram. Since there was no higher mass than 400 amu, it might be that those clusters break up again in the QMS.

Our interferometer acts here as a sensitive mass spectrometer, because it does not need to ionize the molecules like the QMS. After checking that the velocities were as high as expected, the only parameter which remains for variation is the mass. Since it would not have been possible to see the Rhodamine B clusters with an ionizing detector in our setup, this might be a useful feature of the experiment for the future.





4.11.1 Spectrum for 192 °C



4.11.2 Spectrum for 212 °C. The intensity here is by a factor of 1000 higher than in the spectrum measured at a temperature of 192 °C due to the melting point of Rhodamine B at 210-211 °C.

**Figure 4.11:** Mass spectra of Rhodamine B measured at different temperatures. At 192 °C there is one mass peak at 400 amu, at 212 °C there are two mass peaks (at 320 and 400 amu).



# 5 Fluorescence surface detection

In most of the former interference experiments the quantum wave nature of various large molecules was studied using either laser ionization or electron impact ionization in combination with quadrupole mass spectrometry for detecting the interferograms. Surface adsorption in combination with fluorescence detection is a promising alternative, as described in [51], since most ionization detection schemes run into limits when the mass of the particles exceeds  $10^4$  amu [52].

According to the De Broglie wavelength formula, we expect our wavelengths to be in the picometer range. If we, for example, calculate the exact value for TPP, we get

$$\lambda_{DB} = \frac{6.626 \cdot 10^{-34} \text{Js}}{614.74 \cdot 10^{-27} \text{kg} \cdot 187 \text{m/s}} = 5.77 \cdot 10^{-12} \text{m} \quad (5.1)$$

187 m/s is the measured central velocity of the velocity distribution of our molecular beam. As shown in section 1, the separation  $x$  of the interference maxima is

$$x = \frac{L \cdot \lambda_{DB}}{d} = 32 \mu\text{m} \quad (5.2)$$

where  $L$  is the distance between the interference grating and the detection surface.

## 5.1 Imaging

For imaging we used the Zeiss EC Plan-Neofluar  $40 \times$  magnification objective with a numerical aperture of 0.9 and a working distance of 0.41 mm. The numerical aperture is defined as

$$N_A = n \cdot \sin \frac{\phi}{2} \quad (5.3)$$

where  $n$  is the refractive index of the medium in which the lens is working and  $\phi$  is the angular aperture of the lens.

## 5 Fluorescence surface detection

The area of one pixel on the CCD chip is  $0.8 \times 0.8 \mu\text{m}$ .

We had different sets of optical filters, dependent on the molecule and the laser we used. There was one excitation filter placed in front of the glass window of the chamber in order to prevent the ambient light from entering the chamber and to filter side bands of the laser, if there were any. By placing the emission filter between the objective and the tube lens it is ensured that the autofluorescence light from the objective and the chamber is blocked (if it was not in the same range as the fluorescence light the molecules emit) and not adding background light to the images taken. The emission filter was also a bit rotated in order to avoid the Raman scattered light from the entrance window and the quartz plate to enter the chamber.

In figure 5.1 it can be seen how the transmission of an emission filter is changed by rotating it.

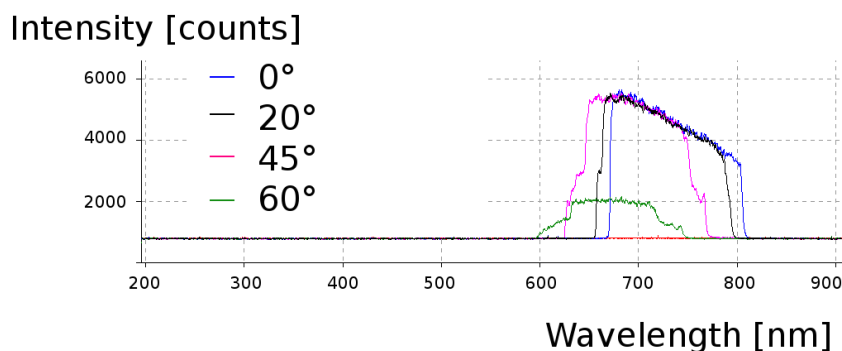


**Figure 5.1:** Transmission of an emission filter when it is rotated. As can be seen in the diagram the transmission can be shifted up to 40 nm at an rotation angle of  $60^\circ$ . The transmission of the filter decreased at an rotation angle of  $60^\circ$  by a factor of 1.8-2.2.

## 5.2 Background signal

For detecting low intensity fluorescence signals, the reduction and subtraction of the background is crucial. The different sources which contribute to the background signal have to be identified and characterized first.

We measured the background with the camera settings used during the experiments.

The background was measured after plasma cleaning the surface at 0.8 mbar. The average number of particles on the surface was about  $0.005/\mu\text{m}^2$  after the cleaning procedure. We focused the objective on the glass slide and the measurement was taken in the center of the field of view. The area we took the data from was  $100 \times 50$  pixel.

With the internal shutter closed the measured mean was 318 with a standard deviation of 36. From the right graph in fig. 2.16 we can conclude that one detected photon corresponds to 8.73 counts. This means that there are about 36 dark counts when applying those setting to the EMCCD camera.

The quartz slide used for this background measurement was coated in such a way that it transmits the fluorescence light of the molecules and reflects the exciting green laser light. The power of the 532 nm laser was constantly increased and the mean and the standard deviation were measured (fig. 5.2). As expected, the mean increased linearly with the power of the laser. The standard deviation followed a square root function (fig. 5.2).

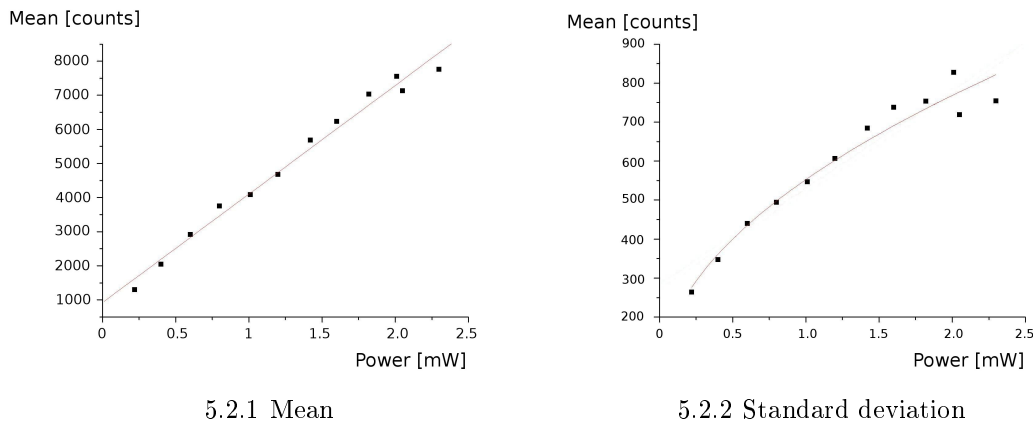


**Figure 5.2:** Background measurements for EMGain 110. As expected, the mean is increasing linearly with the laser power. The standard deviation follows a square root function.

Shot noise, which is caused by the random arrival of photons, is most apparent when collecting a relatively small number of photons. It can be reduced by collecting more photons, either with a longer exposure time or by combining multiple frames.

Each photon is an independent event and the arrival of a single photon cannot be

predicted. Instead, the probability of its arrival in a given time period is governed by a Poisson distribution.

Here, the shot noise can be calculated by the following formula:

$$N_{\text{shot}} = \sqrt{\frac{\text{mean}}{\text{counts/photon}}} \quad (5.4)$$

For the given measurement the shot noise was determined to be more than half of the standard deviation.

Also the background depending on the focusing was measured (fig. 5.3).

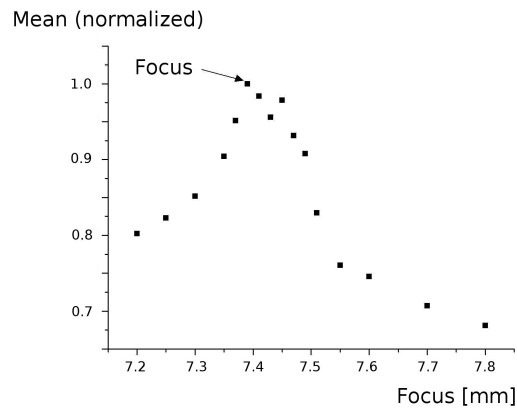


**Figure 5.3:** Background measurements depending on the focusing of the objective. From the focus towards the sides there is an exponential decay. On the vacuum side the mean decreased to 0.78, on the air side to 0.68 of the maximum.

On the left side in fig. 5.3 the focus was on the vacuum side, on the other on the outside of the vacuum chamber. There is an exponential decay from the focus to both sides of the quartz slide. On the vacuum side the mean decreased to 0.78, on the air side to 0.68 of the maximum. Bleaching was irrelevant, because the spot where the background measurements were taken was already completely bleached.

We performed more detailed background studies to compare the backgrounds for the slide used for the green laser, the blue laser and also performed background measurements for an uncoated slide. The CCD settings were as follows: the readout rate was set to 13 MHz, the binning  $1 \times 1$ , the EMGain 110 and the pre-amplifier Gain 4.1. The area the mean was calculated from was  $512 \times 512$  pixel and we used a Zeiss EC Plan-Neofluar

20× magnification objective for this measurement. From our calibration curves we can conclude how many counts correspond to a photon with those settings.

In table 5.1 the results are shown. We measured the background for both the slides used when illuminating the sample with the green laser and the blue laser.

The results from table 5.1 were taken and the ratio of the intensity per photon per pixel and the illumination power per photon per pixel were calculated. The results are shown in table 5.2.

### 5.2.1 Stray light

Stray light is an external noise source adding to the background. There are two different sources contributing to the stray light. On the one hand, there is the exciting laser which cannot be completely blocked with the filters which are built in. On the other hand, the ambient light from the laboratory and other sources inside the vacuum chamber emitting photons contribute to the stray light. For example, the window where the laser enters the vacuum chamber was also fluorescent and hence, adding to the background.

One bandpass filter was in front of the window where the laser entered the vacuum chamber in order to prevent ambient light to enter the chamber. After the objective there were two more longpass filters.

When we did the illumination from outside the chamber with the red laser, we placed a dichroic beam splitter in the optical path, which reflected the laser on the detection surface and then just let the fluorescence light pass through to the CCD chip. There was again a bandpass filter in front of the beam splitter and two more longpass filters after the fluorescence light passing the beam splitter, so that we could make sure to suppress the ambient light and potentially incoming laser light as much as necessary.

The stray light from other sources but the laser could be reduced by covering the vacuum windows and wrapping all optical pathways in aluminum foil. Performing the measurements in a dark laboratory and switching off the glowing pressure gauge in the vacuum chamber was decreasing the background as well.

5 Fluorescence surface detection

BLUE COATED GLASS			
421 nm laser			
Laserpower [mW]	Mean [counts]	Mean [ph]	Mean [ph]/laser power [ph/px]
122	2530	388	$9.34 \cdot 10^{-16}$
68	1635	251	$1.08 \cdot 10^{-15}$
39	1060	163	$1.22 \cdot 10^{-15}$
18	533	82	$1.33 \cdot 10^{-15}$
532 nm laser			
7.7	6700	1028	$3.10 \cdot 10^{-14}$
3.8	3250	498	$3.05 \cdot 10^{-14}$
1.4	1200	184	$3.06 \cdot 10^{-14}$
GREEN COATED GLASS			
421 nm laser			
Laserpower	Mean [counts]	Mean [photons]	Mean [ph]/laser power [ph/px]
67	7199	1104	$4.84 \cdot 10^{-15}$
33	4025	617	$5.50 \cdot 10^{-15}$
21	2640	405	$5.67 \cdot 10^{-15}$
6	827	127	$6.21 \cdot 10^{-15}$
532 nm laser			
198	133	20	$2.39 \cdot 10^{-17}$
101	76	12	$2.68 \cdot 10^{-17}$
60	48	7.36	$2.85 \cdot 10^{-17}$
UNCOATED GLASS			
421 nm laser			
Laserpower	Mean [counts]	Mean [photons]	Mean [ph]/laser power [ph/px]
118	5309	814	$2.03 \cdot 10^{-15}$
97	4267	654	$1.98 \cdot 10^{-15}$
67	2948	452	$1.98 \cdot 10^{-15}$
32	1470	225	$2.07 \cdot 10^{-15}$
532 nm laser			
93	2472	379	$9.48 \cdot 10^{-16}$
56	1802	276	$1.15 \cdot 10^{-15}$
25	871	134	$1.24 \cdot 10^{-15}$
8.6	323	50	$1.34 \cdot 10^{-15}$

**Table 5.1:** Here, the background comparison for different combinations of quartz slides and lasers are shown. The blue laser is equally well suppressed by the slide coated for the green laser and the blue laser. The green laser is, as expected, better suppressed by the glass slide with the appropriate coating for the green laser. For the uncoated slide the blue laser causes more background than the green laser.



	Illumination power/photon/pixel		
Laser	Uncoated glass	Green coated glass	Blue coated glass
532 nm	$1.00 \cdot 10^{-15}$	$2.50 \cdot 10^{-17}$	$3.00 \cdot 10^{-14}$
421 nm	$2.00 \cdot 10^{-15}$	$5 \cdot 10^{-15}$	$1.00 \cdot 10^{-15}$

**Table 5.2:** In the uncoated glass double as much autofluorescence is caused by the blue as by the green laser. The green coated glass suppresses the green laser by two orders of magnitude better than the blue coated glass the blue laser.

### 5.2.2 Dark counts from the EMCCD

The silicon chip in the EMCCD camera converts photons into free electrons which are read out after amplification as current per pixel. Intrinsic CCD noise or dark counts arise according to processes not related to incoming photons which create a current. This can be thermal excitation of an electron or free currents coming up during the readout process.

The camera's quantum efficiency is at its maximum for photons in a wavelength range from 400 to 800 nm (the graph can be seen in fig. 5.4).

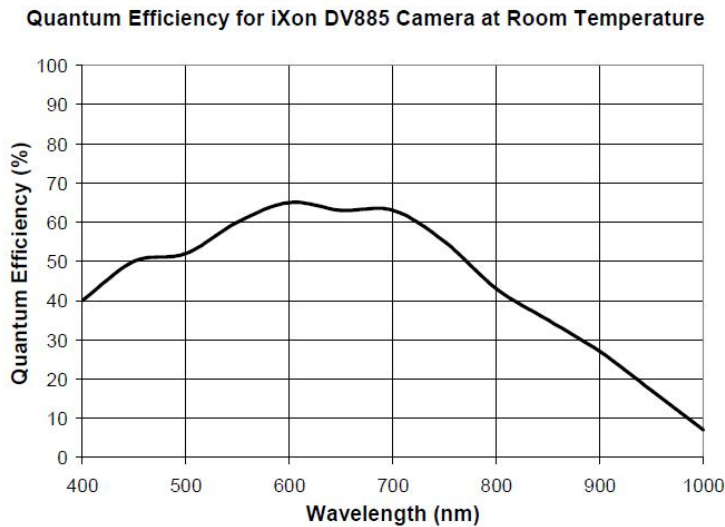


**Figure 5.4:** The quantum efficiency for the Andor Solis DV885. For the wavelengths of the lasers we used and the fluorescent light the molecules were emitting the quantum efficiency was always above 50%. [37]

The dark count rate  $N_{\text{dark}}$  we define as the number of counts per pixel in absence of any light entering the camera and reaching the chip. The parts contributing to this

number is a constant bias  $N_{\text{bias}}$  which does not fluctuate, the thermal noise  $N_{\text{thermal}}$  and the readout noise  $N_{\text{readout}}$ . Hence, the dark counts add up to

$$N_{\text{dark}} = N_{\text{bias}} + N_{\text{thermal}} + N_{\text{readout}} \quad (5.5)$$

We cooled our CCD camera down to  $-80^{\circ}\text{C}$  by internal Peltier cooling which again is cooled by a chiller. The readout noise can be decreased by reducing the readout rate.

Throughout our measurements we assumed that the fluorescence properties of the molecules do not change significantly when the temperature of the source is varied. This assumption is supported by the fluorescence emission spectra of TPP that was evaporated at different temperatures, as it is shown in [51]. The emission spectra remained basically unchanged.

### 5.3 Plasma cleaning

An essential requirement for a successful detection is a clean substrate of low self-fluorescence. We use fused silica quartz (Suprasil I.) glass slides of  $170\ \mu\text{m}$  thickness. Once the molecules are deposited on the surface and the pictures needed for the analysis are taken, we also have to clean the slide from the deposited molecules. We apply plasma cleaning to pre-clean and clean the slide, which is a very convenient method due to its simplicity. Philipp Haslinger and Philipp Geyer from the molecular quantum optics group contributed significantly to the installation of the plasma cleaning.

We proceeded in the following way: An electrode was placed 1-2 mm close to the glass from the outside of the vacuum chamber. The chamber was vented to a pressure of about 1-2 mbar. For venting whether nitrogen, oxygen, air and also argon was used. Any gas except of argon mainly induces a chemical reaction on the surface which has to be cleaned. Argon rather causes mechanical sputtering instead of chemical reactions on the surface.

The voltage applied to the electrode was 1.5 kV and 10 kHz. After that the plasma in the chamber close to the electrode was ignited (see fig. 5.5). The molecules of the process gas were ionized and accelerated towards the electrode. In case of argon, the glass was mechanically sputtered clean. In case of oxygen, air or nitrogen it was mainly the chemical reaction which lead to bleaching of the dirt accumulated on the slide which

lowered the mean.

We avoided gases which caused mechanical sputtering because when cleaning the glass slide, it is also quite probable that material from the aluminium plate surrounding the slide and from the vacuum chamber is sputtered. We observed that after using argon as process gas, the slide was covered with fluorescent particles, which were larger than the molecules we usually see. This was an indication for the sputtering of the walls of the vacuum chamber.

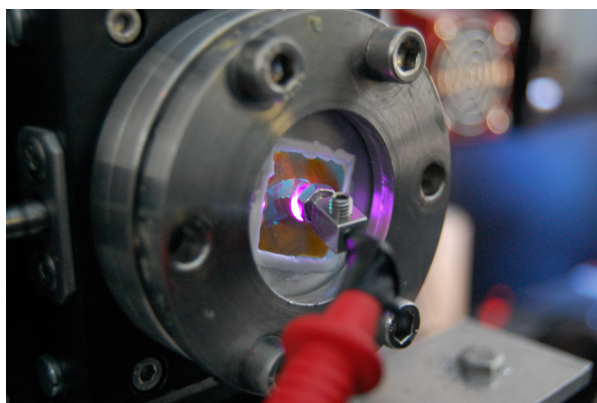


**Figure 5.5:** In this picture the plasma behind the quartz slide can be seen. Depending on the process gas different colours of the plasma were obtained.

The quality of the surface after the cleaning procedure improved significantly. In spite of the reduction of dirt after the cleaning we noticed that the quartz glass has a quite high self-fluorescence. The autofluorescence is much higher when using the laser with shorter wavelength. Therefore, we switched entirely to the red laser when performing single molecule detection.

In order to observe the cleaning process, we used the  $20\times$  magnification objective as the electrode. After checking that the lenses in the objective would stand the voltage without suffering from any kind of damage because of sparks, we were able to observe the cleaning in situ.

In contrast to our expectations, most of the dirt was removed after one second of cleaning. After switching the voltage off, molecules started accumulating again and thus the mean of the image started to increase.

We tried the same cleaning procedure for different pressures and then kept track of the molecules accumulating again on the slide for about ten minutes. The cleaning was

## 5 Fluorescence surface detection

done at a pressure of 5 mbar with air as process gas and the voltage was applied to the electrode for 20 seconds. After that the chamber was pumped again.

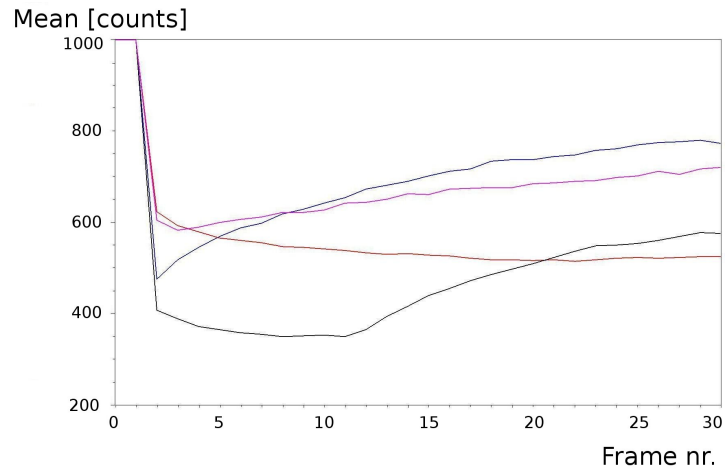


**Figure 5.6:** The red graph indicates the mean at a pressure of 5 mbar, the pink one at 0.1 mbar, the blue graph was measured at a pressure of  $5 \times 10^{-5}$  mbar and the black one at 12 mbar until frame 12 and then the chamber was again pumped to  $5 \times 10^{-5}$  mbar.

As can be seen in fig. 5.6, the slopes are changing for the different pressures and the level from where the mean starts is lower after each cleaning cycle. For the high pressure, thus, the red curve, the mean is constant. The dirt just seems to accumulate if the mean free path is big enough. Also, in the black curve the mean stays the same as long as the pressure is kept high. As soon as it decreased, the mean started to increase. The slope for higher pressures is less steep compared to slopes for lower pressures (comparing the blue and the pink graph in fig. 5.6).

We repeated the measurements and did the cleaning at a pressure of 1 mbar with air as process gas.

As can be seen in fig. 5.7, the mean is always increasing except for a pressure of 1 mbar, where it is actually even decreasing (due to bleaching of the molecules). The slopes of the curves in fig. 5.7 were estimated and plotted as a function of the pressure (fig. 5.8).

The maximal slope was obtained at a pressure of 0.1 mbar. At this pressure the mean free path is 10 mm.

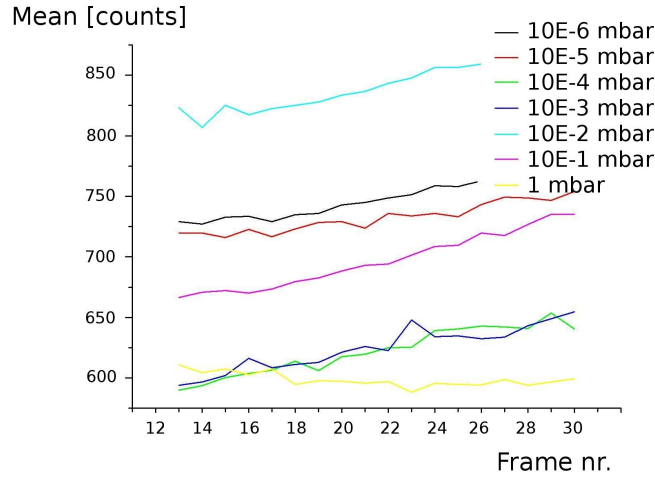


**Figure 5.7:** The quartz slide was plasma cleaned at 1 mbar and the accumulation of molecules measured for different pressures. The mean is always increasing except for a pressure of 1 mbar.

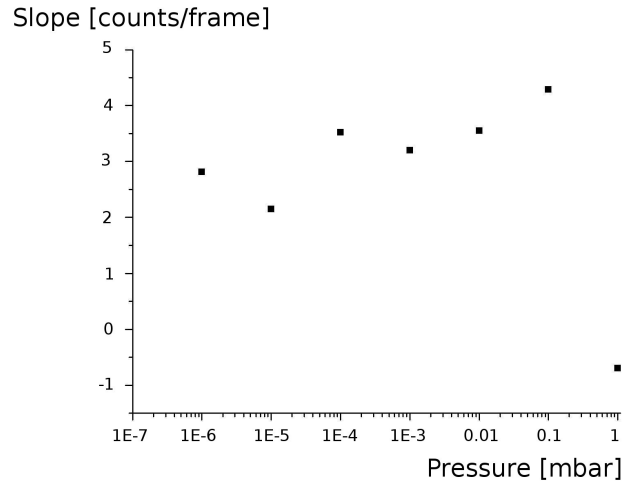


**Figure 5.8:** The slopes of the curves in fig. 5.7 were estimated and plotted as a function of the pressure. It can be seen that for pressures between  $10^{-6}$  and 0.1 mbar the accumulation over time is increasing. For 1 mbar it dropped due to the mean free path which so small at this pressure, that the molecules could not reach the quartz slide to sputter it clean.

In order to check whether the accumulating dirt on the slide was charged or not we applied a voltage to the aluminium plate the slide is glued to and another aluminium plate with a hole as big as the hole for the glass slide, which we put between the chamber and the sample. We isolated the plates from each other and from the vacuum chamber by putting in two rubber rings. It was important to clean this additional aluminium

plate in the ultrasonic bath for about 5 minutes before mounting it to the chamber.

The plasma cleaning was done at a pressure of 1 mbar. After the cleaning the chamber was pumped to 0.2 mbar and the pressure was kept constant. Each 20 seconds an image was taken and the mean of the image estimated (fig. 5.9).

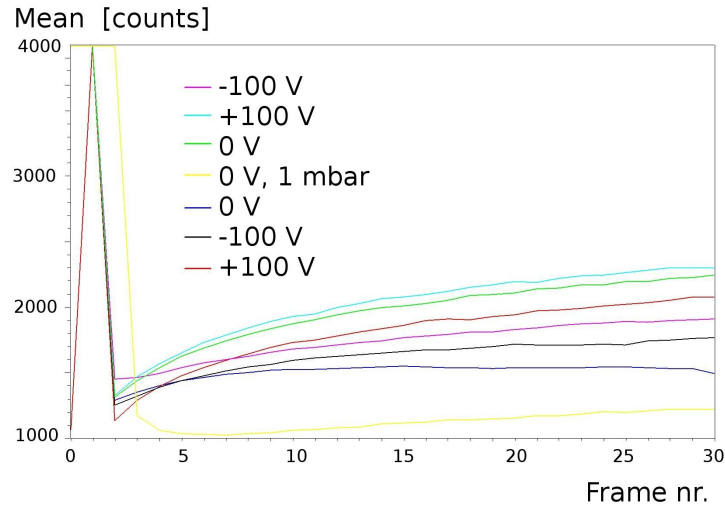


**Figure 5.9:** The first four measurements are done with a voltage applied to the two aluminium plates, in the last two measurements the sample was at the same potential as the vacuum chamber. The cleaning (peak in the first frame) was done at a pressure of 1 mbar for 20 seconds. After that the chamber was pumped to 0.2 mbar and the pressure was kept constant. No systematic dependence of the mean of the picture on the applied voltage was observable.

We could not obtain any systematic behaviour of the slope of the mean depending on the voltage. Hence, the voltage applied to the aluminium plate was irrelevant for the plasma cleaning.

The chamber was baked in order to reduce the dirt accumulations. For that purpose, we installed two Solano halogen bulb lamps with a power of 500 W in the detection chamber and performed five heating cycles of 6 seconds. When the bulbs were switched on for a longer time the temperature of the inside of the chamber was getting too high and we were risking that the pressure gauge gets overheated.

After baking the chamber several cleaning procedures with different process gases were accomplished (fig. 5.10).

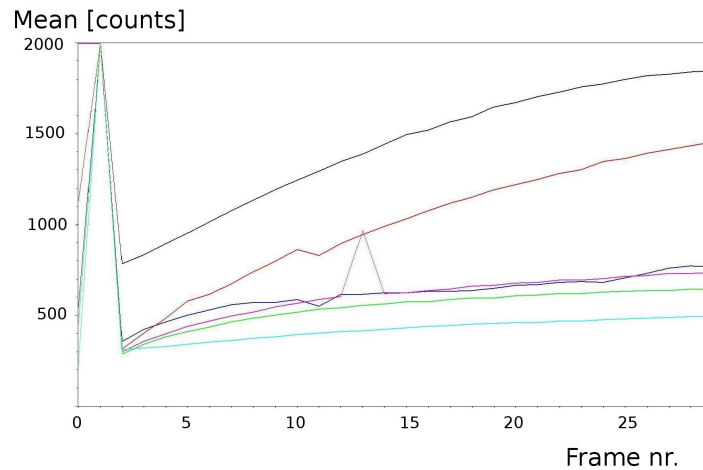


**Figure 5.10:** The cleaning for all curves was done at a pressure of 1 mbar for just 2 frames. After that the accumulation was observed at a pressure of  $3 \times 10^{-5}$  mbar. For the blue and the pink curve the cleaning was done with air, for the red and the black with argon and the turquoise and the green with nitrogen. The slopes for air and nitrogen were approximately the same, for argon the mean increased faster.

The first frame was taken during the cleaning. The mean of the picture is very high due to the ignited plasma.

When using argon as process gas the mean was increasing much faster. The oxygen contained in the air helps the bleaching of the dirt on the surface when using air as process gas. The slope of the green and the turquoise curve for which the cleaning was done with nitrogen is as high as when cleaning with air. The peak in the pink curve was due to a short rise of the pressure to 0.1 mbar. Here, the strong dependence of the mean on the pressure can be seen.

The mean for fig. 5.10 was measured with an EMGain of 110. The mean for fig. 5.6 was measured at an EMGain of 150. Hence, in the last measurement ten times more particles are accumulating on the surface.

While measuring the mean pictures of the quartz slide were taken. Three pictures of those sequences can be seen in fig. 5.11.

Plasma cleaning the aluminium plate and the slide did help to keep the accumulation

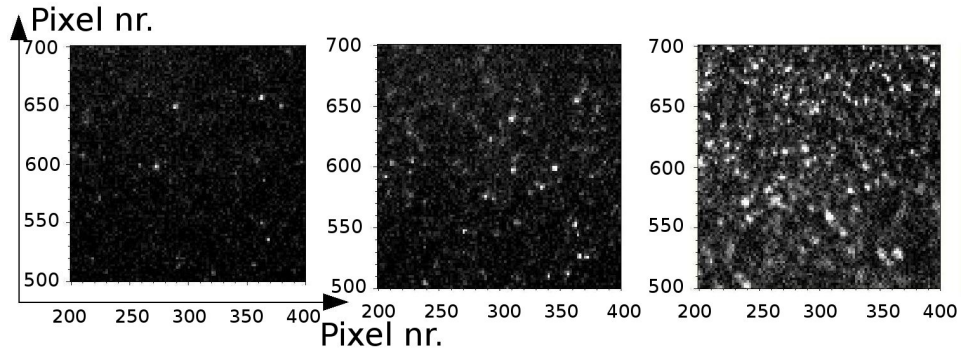


**Figure 5.11:** The accumulation of particles on the glass slide over time is shown. The EMGain setting was 150, each three minutes one frame was taken.

rate low, as can be seen in fig. 5.12. Also, baking the chamber before doing the plasma cleaning is a quite effective method to reduce the increase of the mean.

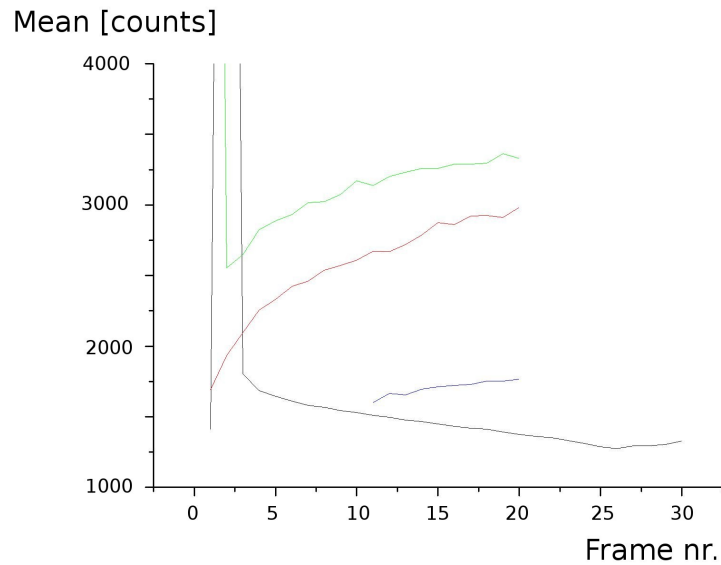


**Figure 5.12:** The red and green curve were measured without plasma cleaning the aluminium plate the quartz slide is glued to. The black curve was measured under the same conditions as the curves in fig. 5.7. The blue curve was measured after plasma cleaning the aluminium plate.

The lowest accumulation rate was obtained after first plasma cleaning the aluminium plate to which the quartz plate was glued to. As process gas air or nitrogen was used, the pressure was kept constant at around 1 mbar. After that the chamber was baked in a couple of short consecutive cycles with a maximal length of six seconds. Before starting a new heating cycle we waited for the temperature to drop down to room temperature



again. Then, the quartz plate was plasma cleaned at around 1 mbar with air or nitrogen as process gas.

## 5.4 Molecular number density

To estimate the number of monolayers of molecules in the time of irradiation at a given temperature of the oven, we refer to the following equation, where the flux is given as:

$$N_{mol} = 8.389 \times 10^{23} \cdot \frac{p[\text{Pa}]}{\sqrt{M[\text{amu}]T[\text{K}]}} \frac{S}{r^2} \left[ \frac{\text{molecules}}{m^2 s} \right] \quad (5.6)$$

The saturation vapor pressure  $p$  can be obtained from extrapolating the vapor pressure curve in [53]. It was determined to be approximately 46.6 Pa. The distance  $r$  between the oven and the quartz surface is 1751 mm, the mass  $m$  of TPP is 615 amu and the oven orifice surface  $S$  about  $1.26 \cdot 10^{-7} \text{ m}^2$ . TPP was evaporated at a temperature of about 670 K. After inserting those values into the previous equation, we also have to include the signal loss due to the gratings and the collimation slits. A rough estimation depending on the grating opening fractions and the opening fractions of the superlattice of the grating leads to an attenuation of about a factor 100. Hence, we get  $3.496 \times 10^{15}$  molecules in one second and one monolayer of TPP after 71 s. One TPP molecule is around  $2 \text{ nm}^2$ , so there are  $2.5 \times 10^{17}$  molecules per  $\text{m}^2$  in one monolayer.



## 6 Interferograms

Before doing the eventual deposition, a test deposition was made with the grating moved out of the beam, but the transversal collimation slits in the beam line. The slits were set to the width later needed for the collimation in the experiment. If molecules were detected on the surface after opening all the valves between the oven chamber and the detection chamber, the beam was adjusted correctly. At this point we also optimized the illumination and adjusted the settings of the camera such as gain and exposure time. In order to get an even illumination, the laser spot was moved with one of the mirrors until it was in the middle of the field of view of the objective.

By doing a test deposition we were also able to predict how much we will have to deposit to see a clear interference pattern. The interference grating attenuates the signal by a factor of 100. Therefore, when doing the actual experiment 100 times more molecules had to be deposited.

When the width of the transversal collimation slits was too small, the width of the deposited stripe started to increase again. It was not clear whether this happened due to increased van der Waals forces, diffraction on the slits or even because Heisenberg's uncertainty relation was coming into play. However, getting the deposited stripe as narrow as possible was always a question of varying the width of the two collimation slits. The narrowest width we could achieve was 6  $\mu\text{m}$ , as shown in fig. 6.1. For this deposition, the first collimation slit was set to a width of 2  $\mu\text{m}$ , the second slit to 1  $\mu\text{m}$ .

There were two ways of detecting an interference pattern. In our first attempts, without being single molecule sensitive, we did the adjustment and then the final deposition. After that we took pictures of the interferogram.

By improving the signal to noise ratio, we were able to see single molecules arriving on the surface. Thus, the detection method changed and we switched to taking pictures during the deposition which allowed us to follow the build-up of the interference pattern.

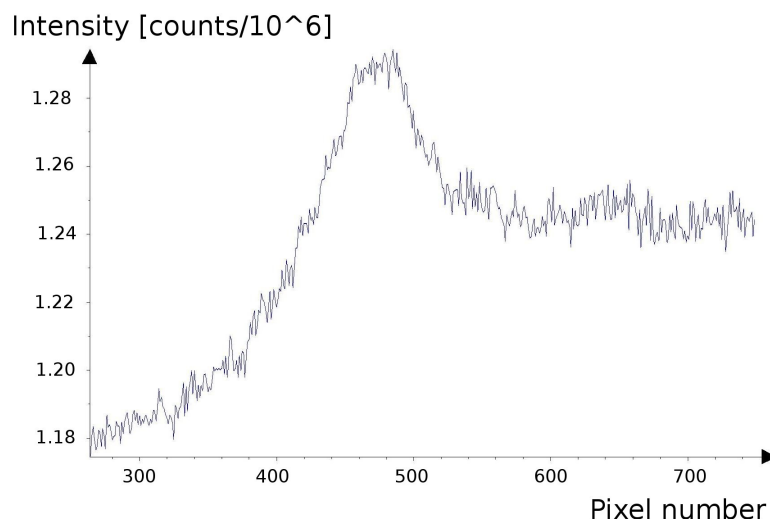


**Figure 6.1:** Here, the vertically binned plot of deposited TPP can be seen. The deposition time was 10 minutes and the deposited amount on the quartz balance  $10 \mu\text{g}$ . The full width half maximum of about 50 pixels translates into  $6 \mu\text{m}$  for the  $40\times$  magnification objective. The higher background on the right side of the stripe is due to an uneven illumination which can be adjusted by shifting the laser spot with one of the mirrors in the optical path.

Since bleaching has a bigger effect in this detection method it has to be taken more into consideration than when applying the other detection scheme. Further details on the detection method applied here are provided in the next section.

Telling apart the molecules arriving from the source from those arriving from the walls of the detector chamber was actually impossible. The particles accumulating even when the valve to the other chambers was closed were fluorescing when illuminated with any laser.

## 6.1 Single molecule detection

Since far-field diffraction is such an intuitive way to understand the wave behaviour of particles, we combined it with the single molecule sensitivity of our setup. This way we were able to observe the molecules arriving one by one on the detection screen and gradually building up the interference pattern.

In the last dozen years the field of single molecule spectroscopy has grown to a powerful technique for exploring the individual nanoscale behavior of molecules in complex local environments. [54, 55, 56]

The main issues we had to deal with on our way to single molecule sensitivity were bleaching of the molecules and the high background due to the autofluorescence of the quartz plate we deposited the molecules on.

By using the Phthalocyanines, which were excited with the red laser, we were able to see single molecules, since the autofluorescence of the quartz glass we deposited the molecules on was much lower. Also, the settings of the EMCCD camera had to be optimized in order to see a single molecule built up of the interference pattern.

The background measurements are as crucial as the measurements done in order to quantify the signal. The number of photons arriving at the chip of the camera were measured for different combinations of lasers and glass slides.

The setup when performing single molecule detection is shown in fig. 2.19.

First, the single photon counting capabilities of our camera were tested. When in single photon counting mode we expected an improvement of the signal to noise ratio (SNR) by a factor of  $\sqrt{2}$  compared to an analog measurement. In order to compare the signal to the background, half of the CCD chip was covered and the other half illuminated by the red laser with 4 mW (fig. 6.2).

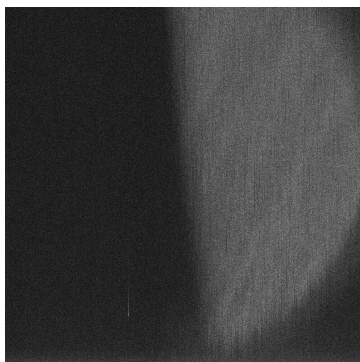


**Figure 6.2:** Here, the measurement of the mean for an illuminated and a dark region is shown. One half of the EMCCD chip was covered, the other half illuminated by the 660 nm laser with 4 mW. The mean was obtained for both regions in order to measure the single photon counting capability of our EMCCD camera and the SNR for the EMGain settings later applied.

The camera was set to single photon counting mode and the threshold was varied. The mean in both the illuminated (ir) and dark region (dr) was measured (see table 6.1).

## 6 Interferograms

Threshold	Mean <sub>ir</sub> ± STDV <sub>ir</sub>	Mean <sub>dr</sub> ± STDV <sub>dr</sub>	SNR
1000	72.4±7.2	48.4 ± 6.1	3.33
1015	44.0±6.5	17.6± 4.1	4.07
1030	36.7±6.1	12.5± 3.6	4.00
1050	34.1±6.0	11.3± 3.4	3.85
1070	29.1±5.5	9.2± 3.1	3.67
1100	26.5±5.3	8.2± 2.9	3.47
1200	17.4±4.3	5.1± 2.3	2.90
1300	13.0±3.7	3.7± 2.0	2.53
analog	2·10 <sup>5</sup> ± 2694	198248 ± 1364	3.03

**Table 6.1:** The illumination time for one frame was 0.4 ms, for one measurement 200 frames were taken. The EMGain was set to 200. The region of interest for the illuminated and dark region was 100 × 100 pixel. In single photon counting mode the noise is close to the square root of the signal. The best signal to noise ratio was obtained for a threshold of 1015. When comparing it to the analog measurement, the SNR was improved by nearly a factor of 1.4.

By varying the threshold we could optimize the SNR. The measurements for various higher EMGains were repeated and we found the maximum of the SNR to be at an EMGain of 220. The SNR increased from 4.07 for an EMGain of 200 to 4.24 for an EMGain of 220.

After knowing the proper settings for the EMGain and the threshold we started a deposition with Phthalocyanine. The chip was uncovered and the deposition started. For 200 seconds each second one frame was taken. The width of the transversal collimation slits was set to 5 μm and the oven temperature to 410 °C. The grating was moved out of the beamline. The flux was so low that it could hardly be measured with the quartz balance (<1 ng/s). In the end of the deposition the amount deposited was about 0.5 μg. The pressure in the oven chamber was 6·10<sup>-7</sup>, the pressure in the main chamber 3.5·10<sup>-8</sup>.

In order to see the deposited stripe the single frames had to be summed up because after each exposure to the laser the arrived molecules bleached. Since the flux was very low, the bleaching rate and the arrival of new molecules where at equilibrium. The sum and the vertically binned plot of the summed up frames can be seen in fig. 6.3.

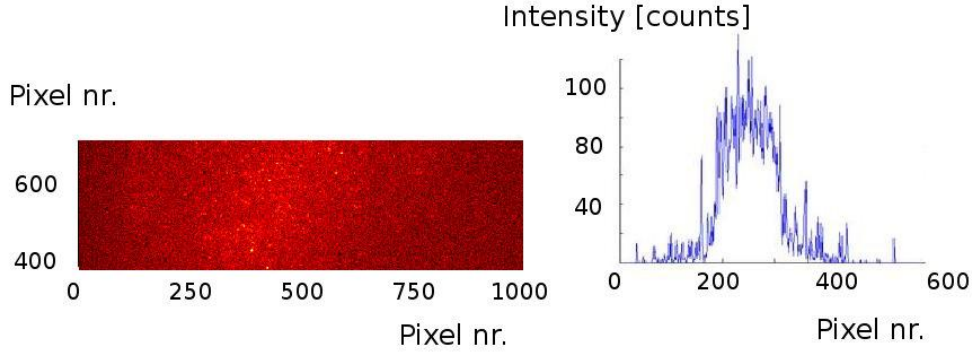


**Figure 6.3:** On the left side the sum of all frames can be seen. The bright spots are single molecules. On the right side the vertically binned plot of the left picture is shown. In the single frames the deposited stripe could not be seen.

## 6.2 Van der Waals interaction

The van der Waals force, named after the Dutch scientist JOHANNES VAN DER WAALS, is the sum of the forces between molecules other than those due to covalent bonds or electrostatic interaction [57]. The interaction includes the force between

- two permanent dipoles
- a permanent dipole and the corresponding induced dipole
- two instantaneously induced dipoles

To estimate the magnitude of the van der Waals force for our experimental setup, we can assume the potential

$$V(r) \propto -\frac{C_3}{r^3} \quad (6.1)$$

for a molecule as close to the grating surface as the van der Waals radius which is about 10 nm. In general  $C_3$  is obtained from the Lifshitz formula [58, 59, 60]

$$C_3 = \frac{\hbar}{4\pi} \int_0^\infty \alpha(i\omega) \frac{\epsilon(i\omega) - 1}{\epsilon(i\omega) + 1} d\omega \quad (6.2)$$

where  $\alpha$  is the dynamic polarizability of the molecule and  $\epsilon$  the dielectric function of the grating material.

## 6 Interferograms

For larger distances retardation of the potential has to be taken into account. The result is the Casimir-Polder potential [61]

$$V(r) \propto -\frac{C_4}{r^4} \quad (6.3)$$

with the constant  $C_4$

$$C_4 = \frac{3\hbar c}{8\pi} \alpha(0) \quad (6.4)$$

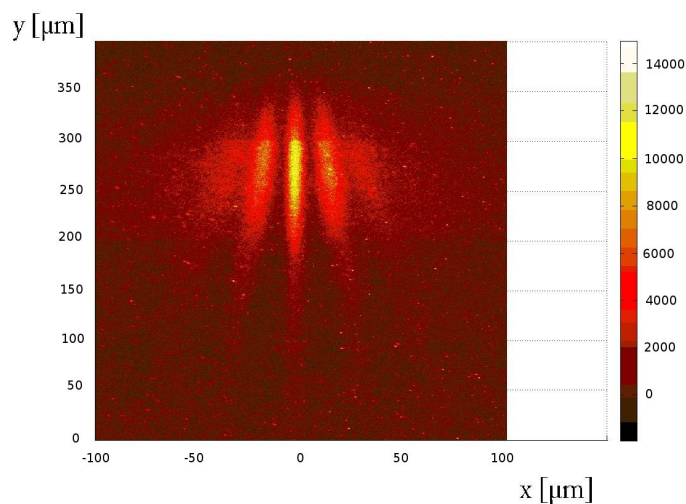
as described in detail in [62].  $\alpha(0)$  is the static polarizability of the particle. Retardation effects show up, when the distance between the particle and the grating walls becomes comparable to the wavelength corresponding to the virtual transitions in the particle that contribute with a large oscillator strength. The two constants  $C_3$  and  $C_4$  can be calculated from the polarizability when assuming that the grating walls are perfect conductors.

Van der Waals interaction in far-field diffraction experiments was already observed with Helium atoms diffracted from nanostructure transmission gratings [14] and with  $C_{60}$  molecules. [63]

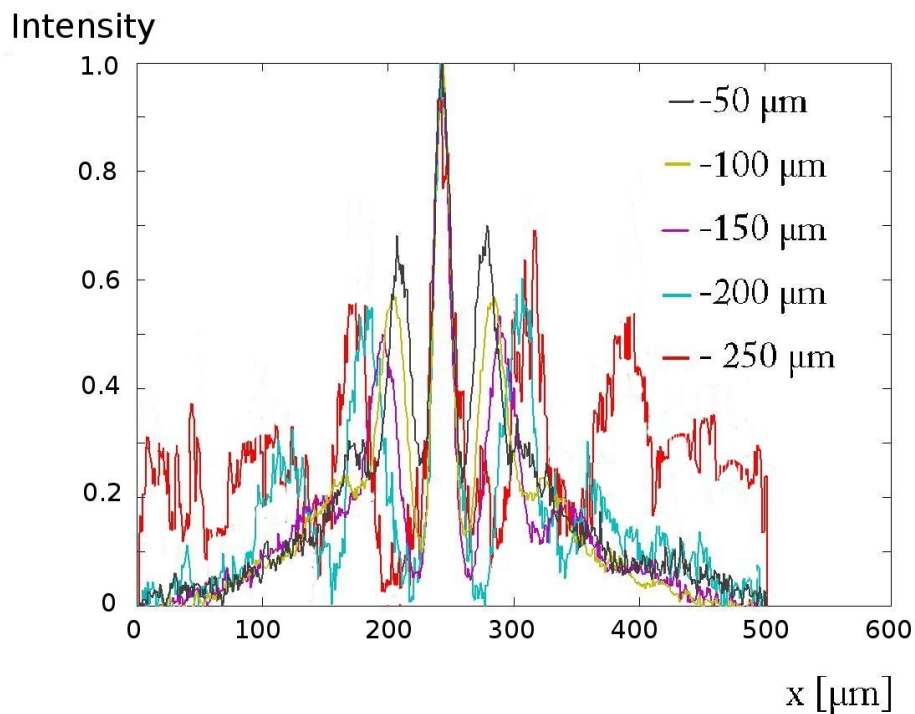
There might be a first indication of the van der Waals force playing a role in our interference measurements. When observing the right picture in fig. 6.4, one can see the vertically binned plot of the interferogram done with TPP on the grating with an opening fraction of 0.5 (top picture). Each horizontal stripe of  $50 \mu\text{m}$  is summed up separately. This way the molecules in the picture are divided by their velocities. For higher velocities, so, for molecules arriving at the top of the screen, the maxima are closer together due to the smaller De Broglie wavelength.

The component where Van der Waals comes into play is the height of the higher order peaks in relation to the zeroth order maximum. For the three bottom stripes, so for the pink, green and red curve, one can see that the height of the first order maximum is getting higher in relation to the central maximum. For the red and the green curve also the second order maxima can be seen. The slower the molecules are, the longer the interaction time with the grating will be and the more the phase shift of the molecules due to the van der Waals interaction will show in the interferograms. That is the reason for the lower part of the interferogram showing the property of more distinct higher





6.4.1



6.4.2

**Figure 6.4:** Interferogram for the grating with an opening fraction of 0.5 and 10 nm thickness. The molecule deposited is TPP. It can be seen that the interference maxima for the faster molecules are closer together due to their smaller De Broglie wavelength. Furthermore, the phase shift imposed by the van der Waals interaction of the molecules with the grating can be seen by comparing the heights of the zeroth and higher order maxima for different velocities.

order peaks, while for the fast molecules, most of the intensity is concentrated in the zeroth and first order maxima.

For the faster molecules, hence for the black and yellow curve, the first order maxima are higher than for the others although they should get smaller. The reason is that the velocity distribution was not taken into consideration for this graph.

### 6.3 Gravitational acceleration

If the grating bars are not aligned perfectly parallel to the vertical direction, two interfering paths can undergo different gravitational shifts. We aligned our gratings to about  $\phi \approx 10^{-3}$  rad, where  $\phi$  is the angle between the grating bars and the gravitational centre. The fringes of the interference pattern can smear out by about  $1 \mu\text{m}$  when assuming that the adjustment was done with an accuracy of 1 mrad.

The adjustment of the gratings was done outside the vacuum chamber. The light of a laser pointer was diffracted on the superseding structure of the interference gratings. It is orthogonal to the structure on which the molecules are diffracted. Hence, by adjusting the superseding structure to the direction of gravitation we ensured that also the actual interference grating for the molecules was adjusted correctly.

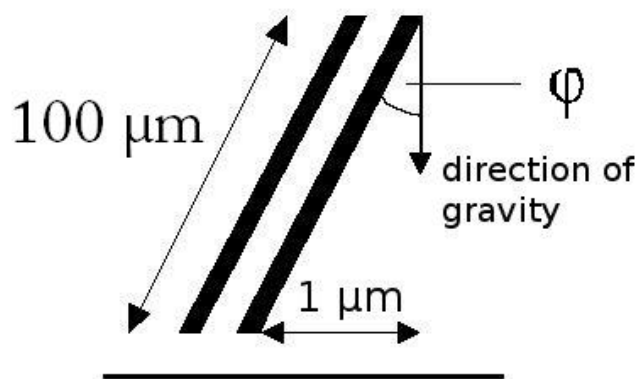


**Figure 6.5:** We aligned the gratings to an accuracy of 1 mrad to the direction of gravitation. The smearing of the interference pattern can be  $1 \mu\text{m}$  at maximum. The distance between the interference peaks is, depending on the molecule,  $15\text{-}25 \mu\text{m}$ . Hence, the smearing due to the gravitational acceleration is for the molecules used so far still negligible.

# 7 Results

## 7.1 Thin gratings

### 7.1.1 Opening fraction $f=0.5$

For the deposition described in this section, the width of the first transversal collimation slit was  $3\ \mu\text{m}$  and of the second slit  $5\ \mu\text{m}$ . The first horizontal collimation slit was  $450\ \mu\text{m}$  wide, the second, which is closer to the grating,  $65\ \mu\text{m}$  wide.

The deposition was done with TPP. We heated the oven to a temperature of  $350\ \text{°C}$ , so we had an average flux of  $21\ \text{ng/s}$ . The experiment took about four hours, in the end an amount of  $300\ \mu\text{g}$  was deposited on the quartz balance.

The pressure in the oven chamber was  $1.4 \cdot 10^{-7}$  mbar, in the interferometer chamber it was  $1.4 \cdot 10^{-8}$  mbar and in the detector chamber  $6 \cdot 10^{-8}$  mbar. The pictures were taken with the  $532\ \text{nm}$  laser at a maximum power of  $100\ \text{mW}$  (after the attenuation by the filters the power exciting the molecules is around  $50\ \text{mW}$ ). The EMGain of the EMCCD camera was set to 110 and the exposure time was 1 second.

As can be seen in the pictures we were able to see the interference maxima up to the third order. The molecules arriving on the top are faster and hence, have less time to fall. Due to the higher velocity, their De Broglie wavelength is shorter and the interference maxima are closer together.

The faster molecules have less time to interact with the grating. Therefore, the phase shift imposed onto them by van der Waals is smaller than for the slow molecules. This can be seen by comparing the intensities of the maxima. For the faster molecules the central maximum is much higher compared to the maxima of higher order. The slower the particles are the smaller the ratio of the peak heights gets.

## 7 Results

The interference picture and the vertically binned plot of the diffraction on this grating are shown in fig. 6.4. The effect described in the previous paragraph can also be seen in this figure. A more detailed description of the graph can be found in the previous section about van der Waals forces.

The velocity distribution for the height from 200 to 250  $\mu\text{m}$  (see fig. 6.4) is shown in fig. 7.1. In the left picture the velocity versus the height at which the molecules arrive is shown, in the right picture one can see the binned plot of the velocities for the selected stripe in the detection plane.

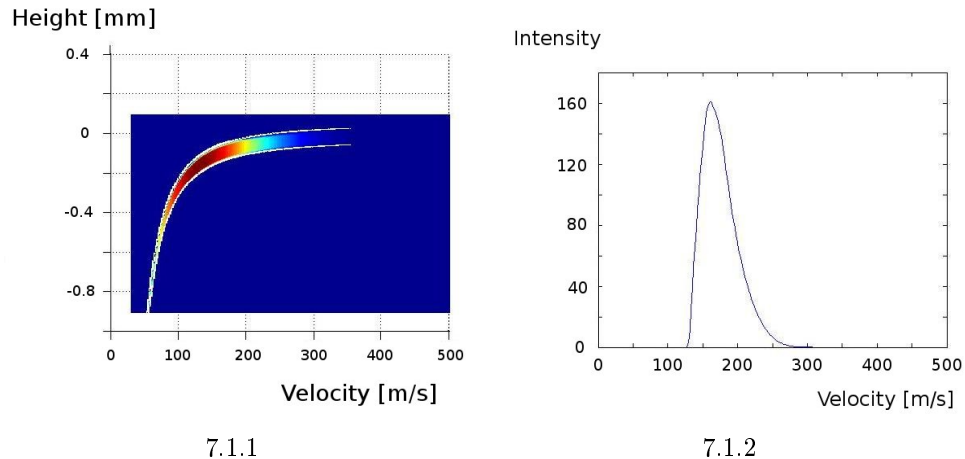


**Figure 7.1:** On the left side the thermal velocity distribution after preselecting with the two horizontal collimation slits is shown for the interferogram done for the grating with an opening fraction of 0.5. On the right side the velocity distribution for the selected stripe in the detection plane is shown.

The fit to the experimental results is shown in fig. 7.2.

### 7.1.2 Opening fraction $f=0.8$

For larger opening fractions we expect the zeroth order maximum to be very intensive, since the envelope of the interference pattern is much narrower. The pattern can be seen in figure 7.3.

The width of the first transversal collimation slit was 4  $\mu\text{m}$ . The grating itself acted as the second slit, because it is written in a  $5 \times 100 \mu\text{m}$  window. There was also a horizontal slit of 60  $\mu\text{m}$  in the beam for the velocity selection. The interferogram was again done with TPP. Hence, the oven was heated up to a temperature of about 380  $^{\circ}\text{C}$ . The pressure in the interferometer chamber was  $3 \cdot 10^{-8}$  mbar, in the oven chamber

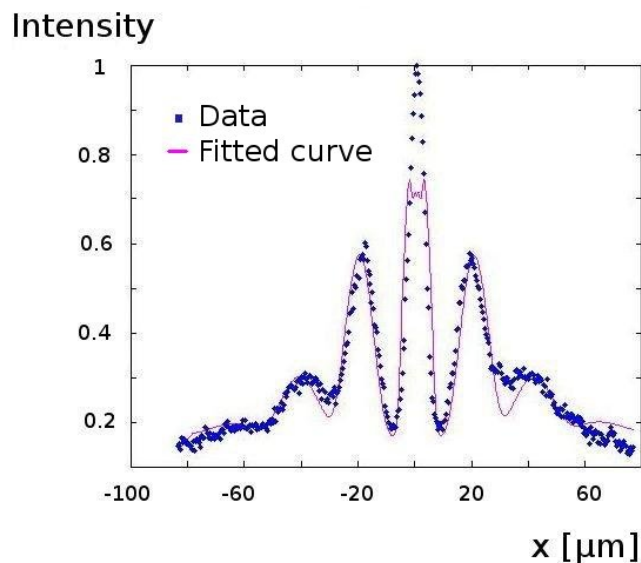
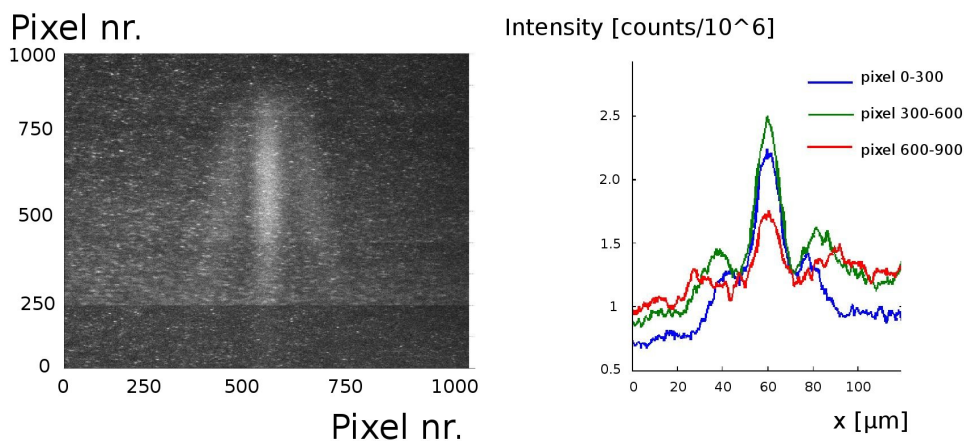


**Figure 7.2:** Here, the data points measured for the grating with an opening fraction of 0.5 and the fit to the data are shown. The maxima of first order are wider apart in the fit. Hence, the velocities calculated are smaller than those in the experiment due to the fact that the height at which the fastest molecules land can just be determined with a certain error.



7.3.1

7.3.2

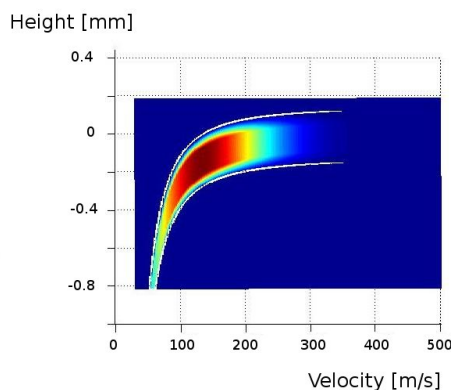
**Figure 7.3:** Interferogram for the grating with an opening fraction of 0.8. For slower molecules which have more time to interact with the grating, the central peak is not as high in relation to the other peaks, because of the phase shift imposed by the van der Waals force.

it was  $1 \cdot 10^{-7}$  mbar and in the detector chamber it was  $2 \cdot 10^{-8}$  mbar. The amount deposited on the quartz balance was  $220 \mu\text{g}$ . The picture on the right side in fig. 7.3

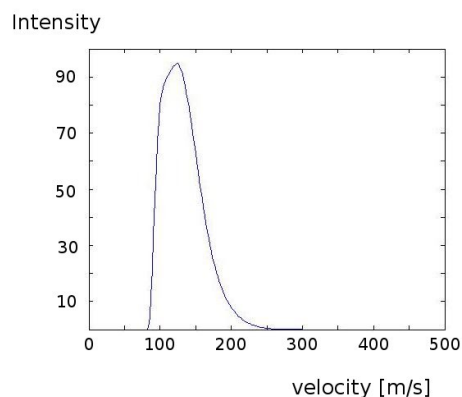
## 7 Results

shows the vertically binned plots of the interferogram for different heights and hence, different velocities. Again, for slower molecules which have more time to interact with the grating, the central peak is not as high in relation to the other peaks, because of the phase shift imposed by the van der Waals force.

The thermal velocity distribution for the height from pixel 250 to 500 (see fig. 7.3) is shown in the right picture of fig. 7.4. In the left picture the velocity versus the height at which the molecules arrive is shown.



7.4.1



7.4.2

**Figure 7.4:** On the left side the thermal velocity distribution of the interferogram done with the grating with an opening fraction of 0.8 is shown. On the right side the velocity distribution for a horizontal stripe of 50  $\mu\text{m}$  height in the detection plane is shown.

The fit to the experimental results can be seen in fig. 7.5.

$C_3$  was fitted and determined to be 19. That matches quite well with the result for the grating with  $f=0.5$  ( $C_3=14$ ).

## 7.2 Thickness 170 nm, opening fraction 0.75

The grating used for the deposition described in this section is 17 times thicker than the other two gratings. The opening fraction was  $f=0.75$ .

The molecules used were TPP and Rhodamine B. The interferogram and the vertically binned plot for TPP are shown in fig. 7.6.

On the left side of the graph the peaks of second order for the slow molecules can be seen. For the fast molecules most of the intensity is concentrated in the central

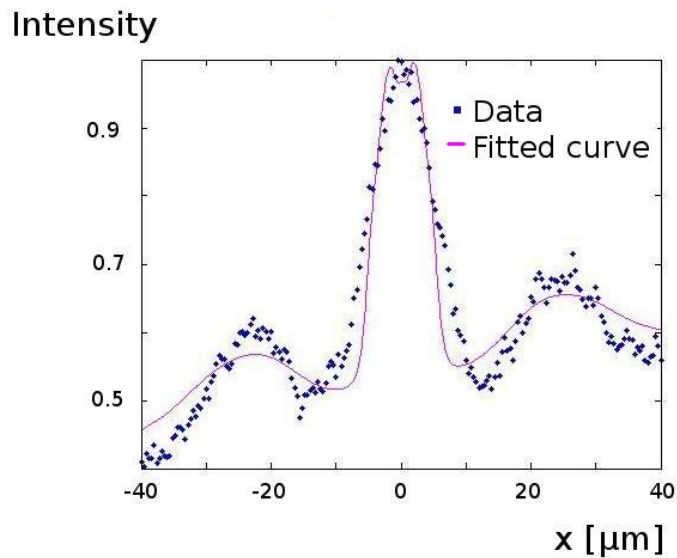
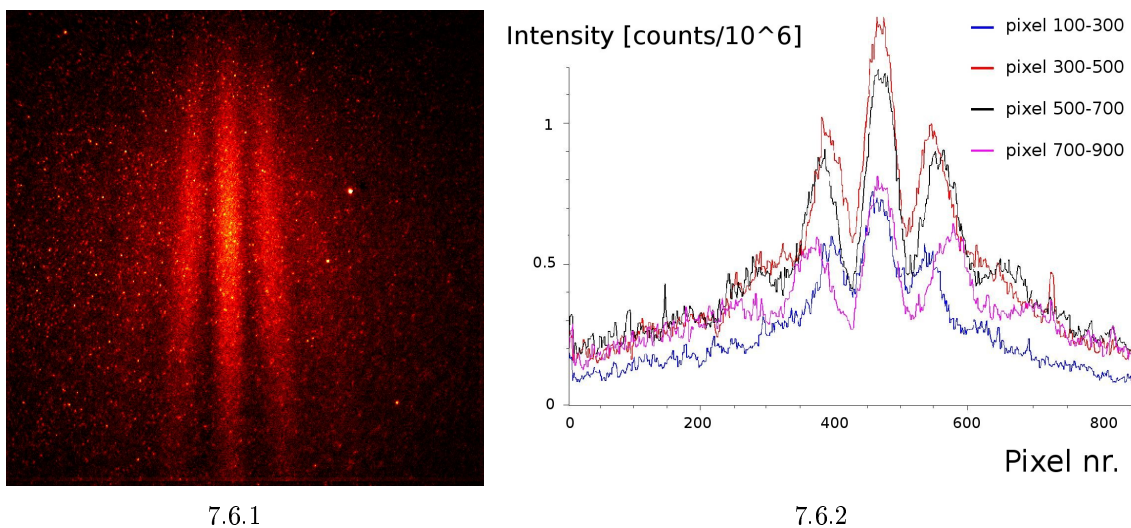


**Figure 7.5:** Here, the data from the interferogram measured with the grating with an opening fraction of 0.8 are shown. Due to the fact that for the considered height the velocity distribution is quite broad, the fit is smeared out at the first order maximum. In order to compensate the smearing, the fit is narrower around the zeroth order maximum.



7.6.1

7.6.2

**Figure 7.6:** Interference of TPP on the 170 nm thick grating. For the fast molecules, most of the intensity is concentrated in the zeroth order maximum.

maximum.

The fit to the experimental results is shown in fig. 7.7.

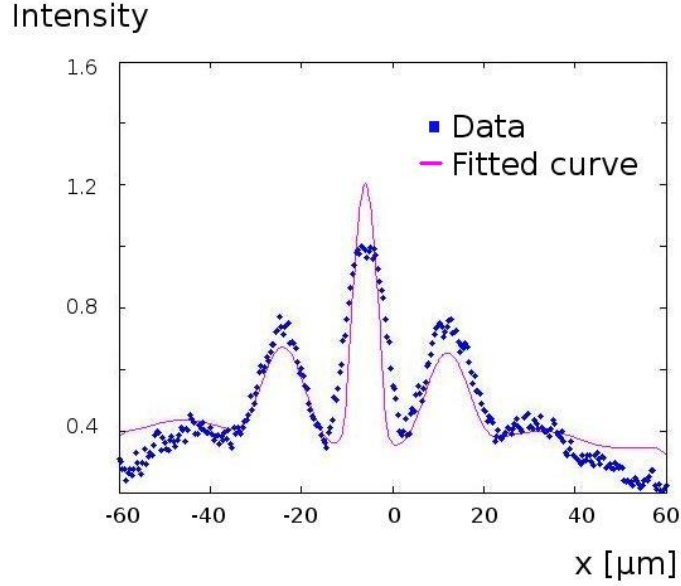


**Figure 7.7:** Here, the experimental data and the fit of the diffraction of TPP on the 170 nm thick silicon nitride grating is shown.

In the fit  $C_3$  was determined to be 130. This is by one order of magnitude higher than for the other two gratings, although in all cases TPP was used and  $C_3$  is only dependent on the molecule's static polarizability.

An explanation might be that due to the grating thickness, the molecule needs more time to pass the grating and hence, can get closer to the grating walls. This might impose a greater phase shift on the molecule and results in a higher  $C_3$  constant.

The velocity distributions are shown in fig. 7.8.

With this grating interference with Rhodamine B was also successfully observed (fig. 7.9).

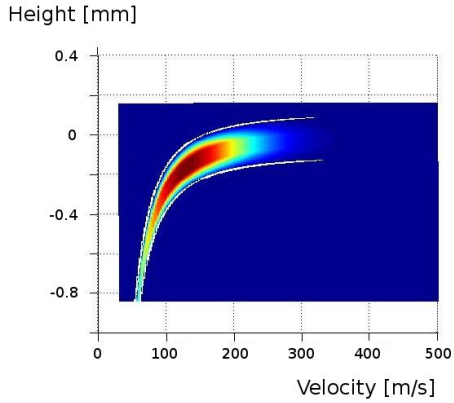
The De Broglie wavelength for Rhodamine B for the velocity measured in the TOF is

$$\lambda_{DB} = \frac{h}{479 \text{amu} \cdot 187 \frac{\text{m}}{\text{s}}} = 4.42 \text{pm}. \quad (7.1)$$

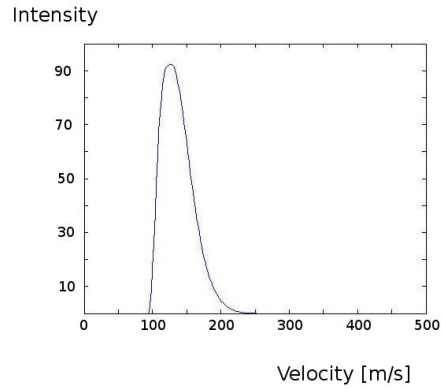
The expected distance between the peaks on the screen is  $x = \lambda_{DB} \cdot L/g = 4.42 \cdot 10^{-12} \text{m} \cdot 0.59 \text{m} / 100 \cdot 10^{-9} \text{m} = 26.1 \cdot 10^{-6} \text{m} = 26.1 \mu\text{m}$ .

The distance measured in the interferogram was  $17.4 \mu\text{m}$ .



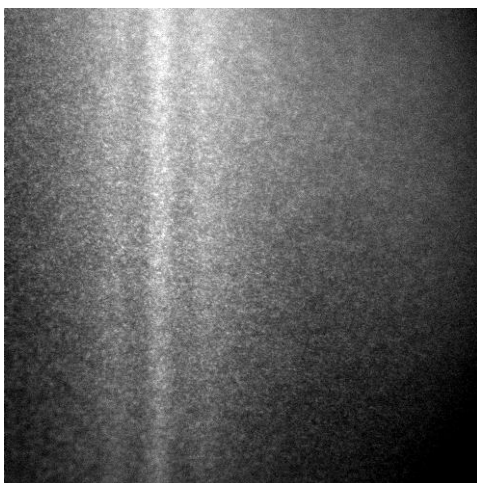


7.8.1

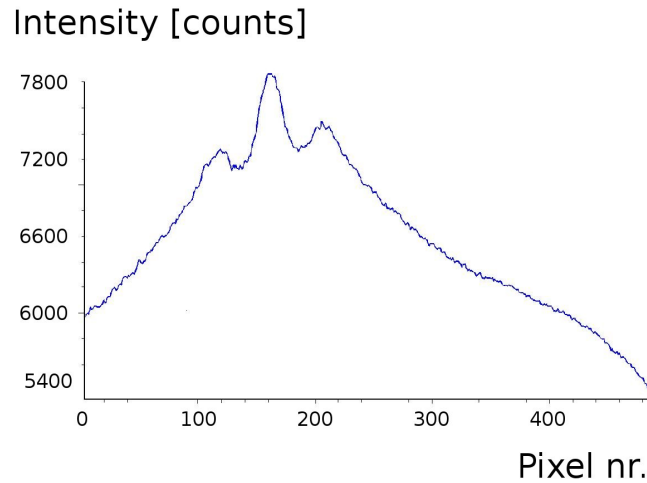


7.8.2

**Figure 7.8:** The velocity distribution for the selected horizontal stripe of  $50 \mu\text{m}$  height in the detection plane is shown on the right side. In the left picture the velocity versus the height can be seen.



7.9.1



7.9.2

**Figure 7.9:** Interferogram of Rhodamine B on the 170 nm thick grating. The width of one pixel is  $0.02 \mu\text{m}$ . The separation of the interference maxima is  $17.4 \mu\text{m}$  and not, as expected,  $26.1 \mu\text{m}$ . The illumination was not perfect as can be clearly seen in the left picture. The high background can be seen in the vertically binned plot, shown in the right picture.

The separation of the maxima was not as expected because Rhodamine B clustered together in our source. As the molecule mass gets bigger, the De Broglie wavelength is getting smaller. The Rhodamine B clusters could not be observed in the quadrupole mass spectrometer because they brake up during the ionization process. Since our detection

## 7 Results

scheme did not require ionization the Rhodamine B clusters did not decompose and could be indirectly detected by calculating the mass of the interfering particles from the separation of the interference maxima.

## 8 Outlook

The observation of the build-up of the interference pattern by single molecules is a pedagogically valuable result. Seeing the molecules making up an interferogram reveals their wave behaviour. At the same time the single molecule detection demonstrates their particle nature. Therefore, the experiment is an intuitive proof of the wave-particle duality of quantum objects.

As always in our interferometer experiments, we want to go to higher masses and hence, bigger molecules. It is convenient for our detection method to use functionalized Phthalocyanines fabricated by Marcel Mayor in Basel, since their absorption maximum is at about 660 nm. In this wavelength range very little autofluorescence in the detection quartz slide and the filters is caused by the lasers.

There are other molecules which are suitable for our detection method like the functionalized Porphyrins. Unfortunately, we have not been able to evaporate them in a proper way for the experiment up to now.

The source we have been using so far leaves room for further improvement. The difficulties we had to deal with were described in chapter 2.

Especially for molecules which could decompose when heated in the thermal source, a new laser evaporation source was implemented. By evaporating molecules from a glass window with a focused laser we can reduce the heat load to a minimum. Temperatures of up to hundreds of Kelvin can be reached in this way. The advantage is that only particles in the area of the focus of the laser beam are affected. This reduces the heat load imposed on the whole vacuum chamber and the molecules by 2-3 orders of magnitude. A further improvement when using this source is that it is as small as the area of the focus of the laser beam. Hence, the spacial coherence is much better than when using the Knudsen cell which had an orifice of about 400  $\mu\text{m}$  in diameter.

In order to reduce the velocity spread a chopper will be added to our setup. For the results shown in this thesis the thermal velocity spread was about 60 % without any

## 8 Outlook

horizontal velocity selection and gets narrower in the direction of gravity. With the horizontal collimation slits the spread could be reduced to 30 %. With a chopper it could be reduced down to few percent, which would improve the longitudinal coherence by up to one order of magnitude. Hence, we would be able to see interference fringes of higher order.

The van der Waals forces acting between the molecules and the interference gratings can be reduced by using thinner gratings. Our final aim is a single atomic layer grating. Since graphene is known for being the most stable material, it is reasonable to use it for a grating made of only one or few atomic layers.

With the setup we want to perform holography with molecules. In order to do that it might be changed to a vertical setup to completely get rid of the velocity spread. The mask which we would use in such an experiment is the Fourier transform of the pattern we finally want to «write» with our molecules. The deposition of very fine molecular structures on a surface might open new technical applications in molecular holography.

# Bibliography

- [1] L. de Broglie. Recherches sur la théorie des quanta. *Ann. de Phys.*, 10e serie, t. 3:053608 1–18, 1925. Dissertation.
- [2] C. Davisson, L. H. Germer. Diffraction of electrons by a crystal of nickel. *Phys. Rev. Lett.* 30, 6, 1927. doi:10.1103/PhysRev.30.705.
- [3] T. Young. Lectures on natural philosophy. Bd. 1, 1807.
- [4] C. Brukner, A. Zeilinger. Diffraction of matter waves in space and in time. *Phys. Rev. A*, 56:3804, 1996.
- [5] M. Arndt, M. Dahan, D. Guéry-Odelin, M. Reynolds, J. Dalibard. Observation of a zero energy resonance in cs-cs collisions. *Phys. Rev. Lett.*, 79:625–629, 1997.
- [6] M. Arndt, L. Hackermüller, K. Hornberger, A. Zeilinger. Organic molecules and decoherence: Experiments in a molecule interferometer. *Birkhäuser, Boston*, 671-10, 2004.
- [7] I. Estermann, O. Stern. Beugung von molekularstrahlen. *Z. Physik*, 61:95–125, 1930.
- [8] H. Halban Jr, P. Preiswerk. Preuve expérimental de la diffraction des neutrons. *Comptes Rendus Acad. Sci. Paris*, 203:73–75, 1936.
- [9] C. G. Shull. Single-slit diffraction of neutrons. *Phys. Rev.*, 179:752, 1969.
- [10] H. Rauch, A. Werner. Neutron interferometry: Lessons in experimental quantum mechanics. *Oxford Univ. Press*, 2000.
- [11] A. Zeilinger, R. Gähler, C. G. Shull, W. Treimer, W. Mampe. Single- and double-slit diffraction of neutrons. *Rev. Mod. Phys.*, 60:1067–1073, 1988.

## Bibliography

- [12] C. Ekstrom, J. Schmiedmayer, M. Chapman, T. Hammond, D. Pritchard. Measurement of the electric polarizability of sodium with an atom interferometer. *Phys. Rev. A*, 51:3883–3888, 1995.
- [13] T. L. Gustavson, P. Bouyer, M. A. Kasevich. Precision rotation measurements with an atom interferometer gyroscope. *Phys. Rev. Lett.*, 78:2046–2049, 1997.
- [14] R. E. Grisenti, W. Schöllkopf, J. P. Toennies, G. C. Hegerfeldt, T. Köhler, M. Stoll. Determination of the bond length and binding energy of the helium dimer by diffraction from a transmission grating. *Phys. Rev. Lett.*, 85:2284–2287, 2000.
- [15] C. Bordé, N. Courtier, F. D. Burck, A. Goncharov, M. Gorlicki. Molecular interferometry experiments. *Phys. Lett. A*, 188:187–197, 1994.
- [16] M. S. Chapman, C. R. Ekstrom, T. D. Hammond, R. A. Rubenstein, J. Schmiedmayer, S. Wehinger, D. E. Pritchard. Optics and interferometry with  $\text{Na}_2$  molecules. *Phys. Rev. Lett.*, 74:4783–4786, 1995.
- [17] B. Brezger, L. Hackermüller, S. Uttenthaler, J. Petschinka, M. Arndt, A. Zeilinger. Matter wave interferometer for large molecules. *Phys. Rev. Lett.*, 88:100404, 2002.
- [18] L. Hackermüller, K. Hornberger, B. Brezger, A. Zeilinger, M. Arndt. Decoherence in a talbot lau interferometer: The influence of molecular scattering. *Appl. Phys. B*, 77:781–787, 2003.
- [19] L. Hackermüller, K. Hornberger, B. Brezger, A. Zeilinger, M. Arndt. Decoherence of matter waves by thermal emission of radiation. *Nature*, 427:711–714, 2004.
- [20] D. Giulini, E. Joos, C. Kiefer, J. Kupsch, O. Stamatescu, H. D. Zeh. Decoherence and the appearance of the classical world in quantum theory. *Springer, Berlin*, 1996.
- [21] T. Juffmann, S. Truppe, P. Geyer, S. Deachapunya, H. Ulbricht, M. Arndt. Wave and particle in molecular interference lithography. *Phys. Rev. Lett.*, 103:263601, 2009.
- [22] S. Gerlich, M. Gring, H. Ulbricht, K. Hornberger, J. Tüxen, M. Mayor, Markus Arndt. Wave and particle in molecular interference lithography. *Angew. Chem. Int. Ed.*, 47:6195–6198, 2008.

- [23] M. Arndt, M. Dahan, D. Guéry-Odelin, M. Reynolds, J. Dalibard. Observation of a zero energy resonance in cs-cs collisions. *Phys. Rev. Lett.*, 79:625–629, 1997.
- [24] S. Gerlich, S. Eibenberger, M. Tomandl, S. Nimmrichter, K. Hornberger, P. J. Fagan, J. Tüxen, M. Mayor, M. Arndt. Quantum interference of large organic molecules. *Nature communications* 2, 263, 2011. doi:10.1038/ncomms1263.
- [25] S. Adler. Concerning an heuristic point of view toward the emission and transformation of light. *J. Phys. A*, page 2935, 2007.
- [26] A. Bassi, D.-A. Deckert, L. Ferialdi. *Europhys. Lett.*, 50006, 2010.
- [27] B. Brezger, L. Hackermüller, S. Uttenthaler, J. Petschinka, M. Arndt, A. Zeilinger. Matter wave interferometry for large molecules. *Phys. Rev. Lett.*, 88:100404, 2002.
- [28] P. Wahlbeck. The failure of isotropy of a gas in an effusion cell and the transition region. *Journal of Chemical Physics*, 55:1709–1715, 1971.
- [29] G. Scoles, D. Bassi, U. Buck, D. Lainé. Atomic and molecular beam methods. *Oxford University Press*, Bd. 1, 1988.
- [30] K. D. Carlson, P. W. Gilles, R. Thorn. *Journal of Chemical Physics*, 38:2725–2735, 1963.
- [31] G. A. Bird. Molecular gas dynamics and the direct simulation of gas flows. *Clarendon Press*, 1994.
- [32] M. P. Grams, A. M. Cook, J. H. Turner, R. B. Doak. Microscopic fused silica capillary nozzles as supersonic molecular beam sources. *J. Phys. D: Appl. Phys.*, 39:930–936, 2006.
- [33] [http://www.laseroptik.de/index.php?substrates:transmission\\_curves](http://www.laseroptik.de/index.php?substrates:transmission_curves).
- [34] K. Ferjutz, J. R. Davis. Handbook of welding, brazing and soldering. 6, 1993.
- [35] G. Sauerbrey. Verwendung von schwingquarzen zur wägung dünner schichten und zur mikrowägung. *Zeitschrift für Physik*, 155 (2):206–222, 1959.
- [36] T. A. Savas, S. N. Shah, M. L. Schattenburg, J. M. Carter and H. I. Smith. *J. Vac. Sci. Technol B*, 13:2732, 1995.
- [37] ixon em+hardware manula version 1.1.

## Bibliography

- [38] <http://web.uvic.ca/ail/techniques/epi-fluorescence.html>.
- [39] J. R. Lakowicz. Principles of fluorescence spectroscopy. page 10, 2006.
- [40] J. R. Lakowicz. Principles of fluorescence spectroscopy. page 11, 2006.
- [41] J. R. Lakowicz. Principles of fluorescence spectroscopy. page 770, 2006.
- [42] [http://en.wikipedia.org/wiki/intersystem\\_crossing](http://en.wikipedia.org/wiki/intersystem_crossing).
- [43] K. M. Kadish, K. M. Smith, R. Guilard. The porphyrin handbook. 1–10, 2003.
- [44] K. M. Kadish, K. M. Smith, R. Guilard. The porphyrin handbook. 11–20, 2003.
- [45] L. Hackermüller, S. Uttenthaler, K. Hornberger, E. Reiger, B. Brezger, A. Zeilinger, M. Arndt. Wave nature of biomolecules and fluorofullerenes. *Phys. Rev. Lett.*, 91:73–75, 2003.
- [46] H. Du, R. A. Fuh, J. Li, A. Corkan, J. S. Lindsey. Photochemcad: a computer-aided design and research tool in photochemistry. *Photochemistry and Photobiology*, 68:141–142, 1998.
- [47] P. G. Seybold, M. Gouterman. Porphyrins 13: Fluorescence spectra and quantum yields. *J. Mol. Spectroscopy*, 31:1–13, 1969.
- [48] <http://omlc.org/spectra/photochemcad/html/index.html>.
- [49] R. F. Kubin, A. N. Fletcher. Fluorescence quantum yields of some rhodamine dyes. *J. Luminescence*, 27:455–462, 1982.
- [50] <http://upload.wikimedia.org/wikipedia/commons/1/10/phthalocyanin.png>.
- [51] A. Stibor. Optical methods for macromolecule interferometry. 2005. Dissertation.
- [52] E. Schlag, J. Grotemeyer, R. Levine. Do large molecules ionize? *Chem. Phys. Letters*, 190:521–527, 1992.
- [53] G. L. Perlovich, O. A. Golubchikov, M. E. Klueva. Thermodynamics of porphyrin sublimation. *J. of Porphyrins and Phthalocyanines*, 4.
- [54] W. E. Moerner, D. P. Fromm. Methods of single-molecule fluorescence spectroscopy and microscopy. *Rev. Sci. Instrum.*, 74:3597, 2003.



- [55] T. Basché, W. E. Moerner, L. Kador. Single molecule optical detection, imaging and spectroscopy. *Phys. Rev. Lett.*, 65:2716, 1990.
- [56] W. E. Moerner, D. P. Fromm. Single molecule spectroscopy: Nobel conference lectures. *Springer Series Chem. Phys.*, 67, 2001.
- [57] J. D. van der Waals. Over de continuïteit van den gas- en vloeistofoestand. *Universit t Leiden*, 1873. Dissertation.
- [58] E. Zaremba, W. Kohn. *Phys. Rev. B*, 13:2270, 1976.
- [59] I. E. Dzyaloshinskii, E. M. Lifshitz, L. P. Pitaevskii. *Adv. Phys.*, 10:165, 1961.
- [60] A. D. McLachlan. *Mol. Phys.*, 7:381, 1964.
- [61] H. B. G. Casimir, D. Polder. The influence of retardation on the london-van der waals forces. *Phys. Rev. Lett.*, 73:360, 1948.
- [62] K. Hornberger, J. E. Sipe, M. Arndt. Theory of decoherence in a matter wave talbot-lau interferometer. *Phys. Rev. Lett. A*, 70:053608 1–18, 2004. Preprint arXiv:quant-ph/0407245.
- [63] O. Nairz, M. Arndt, A. Zeilinger. Quantum interference experiments with large molecules. *Am. J. Phys.*, 71:319, 2003.



## 9 Danksagung

Ich möchte mich bei meinem Betreuer Prof. Markus Arndt bedanken, der mir schon in meinen frühen Studienjahren die Mitarbeit in seiner Gruppe ermöglicht hat.

Weiters danke ich Thomas Juffmann, mit dem ich an diesem Experiment mitarbeiten durfte und der mir immer motivierend zur Seite gestanden ist und meine Fragen beantwortet hat.

Meinen weiteren Kollegen aus der Quantengruppe möchte ich für ein tolles Arbeitsklima und viele interessante Diskussionen danken.



# 10 Curriculum Vitae

---

## Personal data

Date of birth **21.05.1988.**  
Parents **Emma and Mirko Milic.**  
Place of birth **Klagenfurt, Austria.**  
Nationality **Austria.**

---

## Education

07/2010-12/2011 **Master thesis in the group Quantum nanophysics and Molecular Quantum Optics of Univ. Prof. Dr. Markus Amdt, Thesis: Fluorescence detection of far-field interference with large molecules.**

10/2011-12/2011 **Internship at CERN in CMS Analysis, Geneva, Switzerland.**

10/2008-07/2011 **Teaching assistant, University of Vienna, Faculty of Physics, Courses: Physics for nutritionists.**

07/2009-08/2009 **Internship in the group of Univ. Prof. Dr. Markus Arndt, Independent work on smaller experiments.**

07/2008-08/2008 **Internship in the group of Univ. Prof. Dr. Markus Amdt, Assistance at the Cluster Interferometer.**

07/2007 **Internship in the group of Univ. Prof. Dr. Markus Amdt, Assistance at the Kapitza-Dirac-Talbot-Lau Interferometer.**

2006-2011 **Study of physics, Faculty of Physics, University of Vienna.**

1998-2006 **High school, Klagenfurt, School leaving examination passed with distinction.**

1994-1998 **Elementary school, Klagenfurt.**